Integrated Control of Individual Plasma Scalars with Simultaneous Neoclassical Tearing-Mode Suppression

Andres Pajares[1], Eugenio Schuster[1], Kathreen E. Thome[2], Anders S. Welander[2], Jayson L. Barr[2], Nicholas W. Eidietis[2], David A. Humphreys[2]

[1]Lehigh University, Bethlehem, PA 18015, USA

[2]General Atomics, San Diego, CA 92121, USA

E-mail: `andres.pajares@lehigh.edu`

Abstract.

A novel integrated-control architecture has been tested in nonlinear, one-dimensional simulations using the Control-Oriented Transport SIMulator (COTSIM) and in DIII-D experiments. Integrated architectures that can perform continuous-mission control while also handling off-normal events will be vital in future reactor-grade tokamaks. Continuous-mission controllers for individual magnetic and kinetic scalars (thermal stored-energy (W), volume-average toroidal rotation (Ω_ϕ), and safety factor profile (q) at different spatial locations) have been integrated in this work with event-triggered Neoclassical Tearing-Mode (NTM) suppression controllers by combining them into an architecture augmented by a supervisory and exception handling system and an actuator management system. The actuator management system, which enables the integration of competing controllers, solves in real time a nonlinear optimization problem that takes into account the high-level control priorities dictated by the supervisory and exception handling system. The resulting architecture offers a high level of integration and some of the functionalities that will be required to fulfill the advanced-control requirements anticipated for ITER. Initial simulations using COTSIM suggest that the plasma performance and its MHD stability may be improved under integrated feedback control. In addition, the integrated-control architecture has been implemented in the DIII-D Plasma Control System (PCS) and tested experimentally for the first time ever in DIII-D in a high-q_{min} scenario, which is a candidate for steady-state operation in ITER.

1. Introduction

Advanced-control techniques will be required during ITER's high-performance operation phase in order to realize the $Q = 10$ mission and/or steady-state operation [1]. However, some of the control challenges that ITER will face have not been fully explored yet in present fusion devices. One of these challenges is the problem of control integration. In an integrated-control design, its different components must communicate with each other, share available actuation resources, and work in a coordinated fashion. Such integration must ensure a robust operation under nominal conditions but also in the presence of off-normal events such as plasma-state changes and hardware failures. Achieving the necessary level of integration of the different components within an advanced-control Plasma Control System (PCS) architecture becomes a necessity to enable fusion and maximize energy production in ITER and future fusion-power plants. The need for an ITER's PCS with a higher degree of integration than present PCSs was already identified during its conceptual design [2]. Nonetheless, the integration endeavor is particularly challenging in ITER, which will make use of more than 40 diagnostic systems in real time, perform many tens of control tasks, and generate hundreds of individual-actuator signals [3]. Such control requirements require the development of novel PCS components that are essential in an integrated-control architecture, such as Supervisory and Exception Handling (S&EH) systems that introduce both off-line and real-time changes in the discharge control priorities, and Actuator Management (AM) systems that enable optimal usage of the available actuators that are shared by the different control algorithms, while also ensuring actuation within physical saturation limits.

Control integration has been successfully employed in other areas including combustion power plants [4] or chemical reactors [5] in which process efficiency and machine protection are vital. In recent years, the fusion community has started to pay attention to the integrated-control problem by developing PCS architectures that include some of the aforementioned components and functionalities [6, 7, 8, 9, 10, 11]. In [6], an integrated architecture with some S&EH and AM functionalities was developed and tested in simulations with the objective of achieving NTM suppression and safety-factor profile (q) control. In [7], integrated control strategies for NTM suppression and β control were tested in the ASDEX-U tokamak together with an Electron-Cyclotron Heating and Current Drive (ECH&CD) management scheme. The work in [8, 9, 10] presents a generic integrated-PCS architecture with special emphasis on its S&EH functionalities [8, 10] and a task-based AM approach [9]. The architecture was tested in the TCV tokamak using up to three ECH&CD launchers and one Neutral Beam Injection (NBI) system, and in ITER simulations using a broader array of actuators [9]. The work in [11] focuses on the development of NTM suppression control-techniques in TCV, and tests them together with regulation of β and a model-estimated q-profile using the PCS architecture from [8, 9]. In other previous work, like [12, 13], integrated controllers are proposed for combined magnetic and kinetic control, although the main elements of an integrated architecture, like S&EH systems and AMs, are not present. In addition, pieces of work like [14, 15] focus solely on the development of S&EH algorithms, whereas other work (e.g. [16]) centers its attention on developing strategies for actuator management.

In the context of developing the necessary integrated-control architectures for present devices and future burning-plasma tokamaks, the main contribution of this work is not the synthesis of individual controllers [17, 18, 19] but the design and experimental testing of an integrated-control architecture powered by an optimization-based actuator management system for simultaneous regulation of kinetic, magnetic, and MHD-related plasma properties. The architecture integrates four types of components: (i) individual controllers for plasma kinetic variables (namely, the thermal stored-energy, W, and the volume-average toroidal rotation, Ω_ϕ [17]), plasma magnetic variables (namely, the central safety factor, q_0, and edge safety factor, q_e [18]), and MHD-related variables (namely, the magnetic island-width w), (ii) controllers for NTM suppression that use localized ECH&CD and are based on active-suppression techniques [20] and pre-emptive stabilization [21], (iii) the Off-Normal and Fault Response (ONFR) system [15], which offers some S&EH capabilities, and (iv) a novel AM algorithm based on nonlinear, real-time optimization. The overall control scheme is nonlinear and robust, and has been designed and tested in one-dimensional (1D) nonlinear simulations and DIII-D experiments using the ohmic coil, NBI systems, and ECH&CD launchers as actuators.

While preliminary ideas and results on optimization-based actuator management were presented in [22, 23], the integrated-control architecture proposed in this work represents a significant generalization effort in many aspects. First, the integrated-control architecture is augmented by incorporating S&EH functionalities (ONFR system). Second, a larger set of both kinetic and magnetic control objectives (e.g., rotation, local values of the safety factor, NTM island width) are simultaneously handled and integrated. Third, not only continuous-mission controllers but also event-triggered controllers (NTM suppression) are integrated under the S&EH and AM systems. Fourth, the real-time optimization-based AM algorithm is now capable of solving not only overactuated but also underactuated problems while at the same time incorporating constraints dictated by the S&EH system. Finally, the control-integration solution presented in this work offers a higher degree of maturity due to its practical implementation in the DIII-D PCS and experimental testing in DIII-D.

The controllers integrated under the proposed architecture in this work are designed to regulate individual-scalar variables (i.e. W, Ω_ϕ, q_0, and q_e) instead of whole profiles‡ as in [19], for instance. This decision responds purely to a controllability issue imposed by the limited actuation capability usually found in tokamaks. As more simultaneous control objectives are added, regulating either the value of the profile at particular spatial locations (e.g. q_0 and q_e rather than the whole q profile) or a spatial average/integral of the profile (e.g. W rather than the whole plasma-pressure

‡ In this context, "whole profile" regulation means that control of a particular profile at a high number of nodes (i.e. so that most of its spatial domain is covered) is attempted.

profile) may be the only attainable goals. This is specially relevant in reactor-grade tokamaks with a higher degree of actuator sharing and a larger number of control tasks. It is important to emphasize, however, that if controllability were not an issue, the integrated-control architecture proposed in this work could also handle controllers designed for "whole profile" regulation. The individual-scalar controllers in this work are synthesized independently of each other by means of zero-dimensional (0D) control-oriented, physics-based models of the plasma dynamics. Uncertainties are included in the control-synthesis models to characterize partial lack of physics modeling and/or knowledge, enabling robust-control design. In addition, NTM-suppression controllers, which have been developed in previous work [20, 21], are included in the integrated-control scheme to steer the ECH&CD toward the location where NTMs are or may be developing. The integration of kinetics, magnetics, and NTM control make this work stand out from previous work focused exclusively on NTM-suppression in DIII-D. Moreover, the design of a nonlinear EC-power controller that ensures a particular rate of suppression represents a novel contribution to present efforts on NTM-suppression integration.

This paper is organized as follows. The overall integrated-control architecture is described in Section 2. The models utilized for control synthesis are presented in Section 3. The components of the control architecture are described in Section 4. In particular, Section 4.1 presents a generic control synthesis of the individual-scalar controllers, Section 4.2 briefly describes the NTM-suppression controllers, Section 4.3 briefly describes the S&EH system, and Section 4.4 introduces the AM algorithm employed in this work. Nonlinear, 1D simulation results using COTSIM© (Control-Oriented Transport SIMulator), which uses simulation models that are significantly more complex [19] than the control-synthesis models in Section 3, are presented in Section 5. Initial DIII-D experimental results are presented in Section 6. Finally, a conclusion and possible future work are stated in Section 7.

2. Overview of the Integrated-Control Architecture for Individual-Scalar Regulation and NTM Suppression

A functional diagram of the PCS architecture developed in this work is shown in Fig. 1. It is considered that the actuators available for control are the ohmic coil, NBIs, and steerable ECH&CD, so that the controllable inputs to the tokamak-plasma system are the total plasma current, I_p, NBI powers, $P_{NBI,i}$ ($i = 1, ..., N_{NBI}$, where N_{NBI} is the total number of NBI groups§), and EC powers and radial location of the localized ECCD, $P_{EC,j}$ and $\hat{\rho}_{EC,j}$, respectively ($j = 1, ..., N_{EC}$, where N_{EC} is the total number of EC launchers). During operation, plasma data is measured in real time by the different diagnostic systems in the tokamak vessel. This data is processed in real time (e.g., profile estimation and/or equilibrium reconstruction), and an estimation the plasma

§ In this work, a group is considered as a set of actuators whose powers are regulated as a single controllable input.

state is sent to the S&EH system as well as to the different feedback controllers (i.e. the individual-scalar controllers and NTM-suppression controllers).

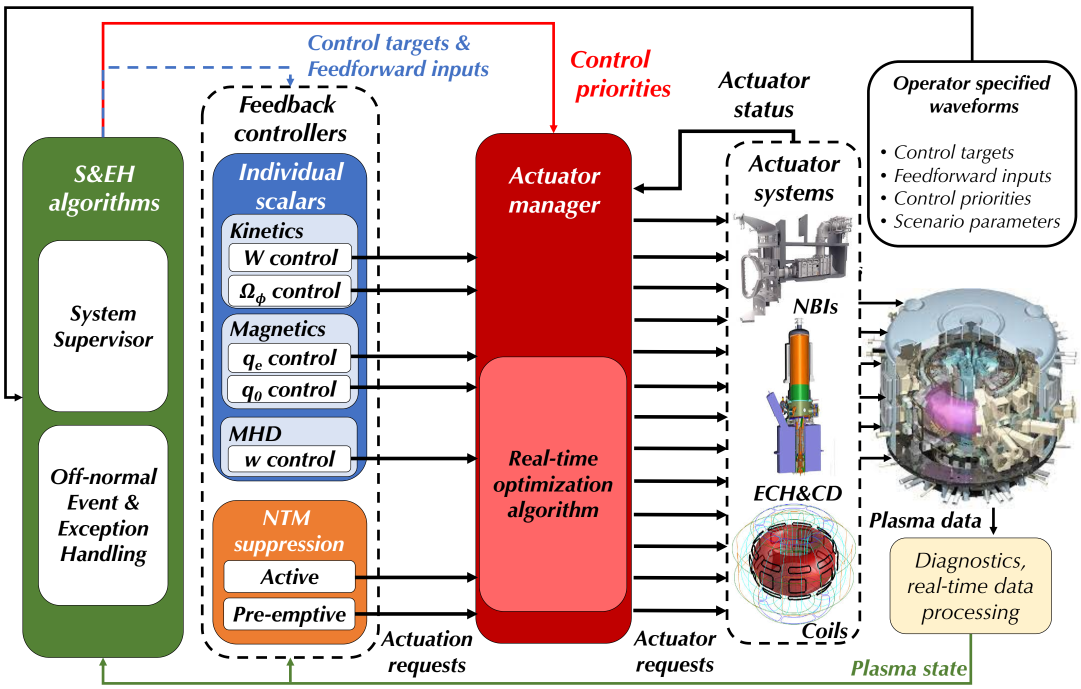

Figure 1: Schematic of the integrated-control architecture developed in this work.

In addition, the S&EH algorithms receive the control targets, feedforward inputs, control priorities, and other relevant scenario parameters as set up by the control operator. The control targets and feedforward inputs may be modified by the S&EH algorithms before they are sent to the feedback controllers. Moreover, the off-line control priorities set up by the control operator (which would usually be related to discharge-phase control requirements) can be updated by the S&EH algorithms in real time when potential off-normal events are identified based on the plasma state.

The individual-scalar controllers and NTM-suppression controllers try to fulfill their particular control goals by computing high-level, individual actuation requests that are functions of I_p, $P_{NBI,i}$, $P_{EC,j}$, and $\hat{\rho}_{EC,j}$, such as, for example, the total injected power necessary for W control, the NBI torque required for Ω_ϕ control, or the localized current deposition desired for q control. These high-level actuation requests are sent to the AM algorithm, which also receives information from the actuator systems (i.e. maximum/minimum physical-saturation limits and actuator failure flags). Together with the control priorities, the AM algorithm computes the low-level actuator requests (i.e. the controllable inputs, I_p, $P_{NBI,i}$, $P_{EC,j}$, and $\hat{\rho}_{EC,j}$) that achieve the high-level actuation requests as closely as possible. This is done by solving a nonlinear-optimization problem in real time. It must be kept in mind that there are other low-level actuator requests (e.g. NBI voltage and modulation timing, ohmic coil current/voltage, etc.) which are essential in terms of actuator safety and reliability. However, in this work, these other low-level actuator requests are considered to be regulated by dedicated actuator hardware-control systems, and not by the PCS itself (although, from a mathematical perspective, the AM algorithm in this work could be employed to handle such AM problems as well).

Some additional considerations about the integrated architecture described in Fig. 1 can be noted. First, the S&EH algorithms do not receive direct information from the actuator systems, and the actuator manager is in charge of dealing with potential actuator failures. Architectures with S&EH algorithms that take into account actuator status may have a higher degree of integration (e.g. [8]). Nonetheless, as shown in Sections 5.2 and 6, the present architecture efficiently manages a large array of actuators both in simulations and DIII-D experiments. Second, the feedback controllers are not resource-aware algorithms, so the responsibility of limiting the actuator commands to physical actuation limits rests entirely on the actuator manager. This is one of the integrated-architecture types envisioned within [16], although other work has also considered schemes with resource-aware controllers [10]. Finally, the architecture is specially designed to use NBI, ECH&CD, and the central solenoid, but its design can be directly extrapolated to tokamaks with other actuators such as ion cyclotron heating or lower hybrid, and other coils.

3. Plasma Models for Control Synthesis

3.1. Central and Edge Safety-Factor Dynamics

The plasma geometry is described by a single spatial coordinate, $\rho \triangleq \sqrt{\frac{\Phi}{\pi B_{\phi,0}}}$, where $B_{\phi,0}$ is the vacuum field at the geometric axis, and Φ is the toroidal flux [24]. The safety factor, q, is defined as

$$q \triangleq -\frac{\rho_b^2 \hat{\rho} B_{\phi,0}}{\partial\psi/\partial\hat{\rho}}, \tag{1}$$

where ψ is the poloidal stream function, $\hat{\rho} \triangleq \rho/\rho_b$, and ρ_b is the value of ρ at the last closed magnetic-flux surface.

The central and edge safety factors, q_0 and q_e, correspond to the value of q at the magnetic axis ($\hat{\rho} = 0$) and plasma edge ($\hat{\rho} = 1$), respectively. Specifying the value of (1) at $\hat{\rho} = 0$ and $\hat{\rho} = 1$ yields

$$q_0 \triangleq -\left.\frac{\rho_b^2 \hat{\rho} B_{\phi,0}}{\partial\psi/\partial\hat{\rho}}\right|_{\hat{\rho}=0} = -\left.\frac{\rho_b^2 B_{\phi,0}}{\partial^2\psi/\partial\hat{\rho}^2}\right|_{\hat{\rho}=0}, \quad q_e \triangleq -\frac{\rho_b^2 B_{\phi,0}}{\left.\partial\psi/\partial\hat{\rho}\right|_{\hat{\rho}=1}}, \tag{2}$$

where L'Hopital's rule has been applied within the definition of q_0.

By means of the magnetic-diffusion equation [24] and the definition of q_0 in (2), a dynamical model can be obtained (the details can be found in Appendix A) as given by

$$\begin{aligned}\frac{dq_0}{dt} &= q_0\lambda_\eta u_\eta + q_0^2\sum_{i=1}^{N_{NBI}}\lambda_{NBI,i}u_{NBI,i} + \\ &+ q_0^2\sum_{j=1}^{N_{EC}}\lambda_{EC,j}(\hat{\rho}_{EC,j})u_{EC,j} + q_0^3\lambda_{BS}u_{BS} + \delta_{q_0} \triangleq j_{q_0} + \delta_{q_0},\end{aligned} \tag{3}$$

where λ_η, $\lambda_{NBI,i}$, and λ_{BS} are model constants, $\lambda_{EC,j}$ are functions of $\hat{\rho}_{EC,j}$, j_{q_0} is an auxiliary variable used to denote the right-hand side of (3) without uncertainties, the variables $u_{(\cdot)}$ are virtual inputs that depend on the controllable inputs (namely I_p, $P_{NBI,i}$, and $P_{EC,j}$) and the line-average electron density, $\bar{n}_e$, as given by

$$u_\eta = (I_p\sqrt{P_{tot}}\bar{n}_e^{-1})^{-\frac{3}{2}}, \qquad u_{BS} = (I_p\sqrt{P_{tot}}\bar{n}_e^{-1})^{-\frac{1}{2}}\,\bar{n}_e \tag{4}$$

$$u_{NBI,i} = (I_p\sqrt{P_{tot}})^{-1}\,P_{NBI,i}, \quad u_{EC,j} = (I_p\sqrt{P_{tot}}\bar{n}_e^{-1})^{-\frac{1}{2}}\,\bar{n}_e^{-1}P_{EC,j}, \tag{5}$$

and δ_{q_0} is a model uncertainty that bundles partially unmodeled sources of current that modify the q_0 dynamics.

In addition, using the boundary condition at $\hat{\rho} = 1$ of the magnetic-diffusion equation (see Appendix A) and the definition of q_e in (2), a dynamical model can be obtained as given by

$$\frac{dq_e}{dt} = -B_{\phi,0}\rho_b^2\left(\frac{1}{k_{I_p}^{nom}I_p^2}\frac{dI_p}{dt} + \delta_{q_e}\right), \tag{6}$$

where $k_{I_p}^{nom}$ is a constant model parameter, and δ_{q_e} is an uncertain term that bundles partially unmodeled changes in the plasma equilibrium.

The inclusion of model uncertainties in this work, like δ_{q_0} and δ_{q_e}, is essential to enable a robust-control design that can deal with realistic limitations in the understanding and modeling of the plasma-physics phenomena. The key idea is that these uncertain terms do not need to be fully known, i.e. closed analytical expressions for them are not needed. As long as upper bounds to their absolute values can be estimated, robust controllers can be synthesized (see Section 4.1). A robust-control design ensures the desired control performance despite the unknown dynamics embedded in the model uncertainties, denoted by $\delta_{(\cdot)}$ along this paper. A broad database exists with shots that are relevant for our scenario of interest, and in which measurements/estimations of the plasma state are available. Therefore, estimating non-conservative upper bounds to $\delta_{(\cdot)}$ is a feasible task. A database composed of 23 DIII-D shots has been employed to estimate $\delta_{(\cdot)}$ and their upper bounds. All shots in the database belong to the DIII-D high-q_{min} scenario [25], which is a potential candidate for the realization of steady-state operation in ITER, and may require current-profile, energy, and NTM control. Due to its relevance, such scenario has indeed been employed for simulation and experimental testing in this work (see Sections 5 and 6, respectively).

3.2. Thermal Stored-Energy Dynamics

A 0D power balance is employed to model the dynamics of W, which is given by

$$\frac{dW}{dt} = -\frac{W}{\tau_E} + P_{tot} + \delta_W, \tag{7}$$

where τ_E is the energy confinement time, which is modeled by the IPB98(y,2) scaling,

$$\tau_E = 0.0562H_{98(y,2)}I_p^{0.93}B_{\phi,0}^{0.15}R_0^{1.97}\epsilon^{0.58}\bar{n}_e^{0.41}\kappa^{0.78}A_{eff}^{0.19}P_{tot}^{-0.69}, \tag{8}$$

where $H_{98(y,2)}$ is the so-called H factor, $\epsilon \triangleq a/R_0$ is the inverse aspect ratio (where a is the minor radius and R_0 is the major radius), κ is the plasma elongation, and A_{eff} is the plasma effective mass [26]. In (7), δ_W is an uncertain term that characterizes unmodeled changes in the plasma confinement (e.g. MHD instabilities, electron runaways, etc.) or sources of power (surges in radiated power and/or ohmic power, changes in auxiliary-source absorption efficiencies, etc.). Just like for δ_{q_0} or δ_{q_e} in Section 3.1, it is assumed that an upper bound to $|\delta_W|$ has been estimated.

3.3. Volume-Average Toroidal-Rotation Dynamics

The volume-average toroidal rotation is defined as $\Omega_\phi \triangleq \frac{1}{V}\int_V \omega_\phi dV$, where ω_ϕ is the ion toroidal-rotation profile. A dynamical model for Ω_ϕ can be obtained (see Appendix B for a full derivation of this model) as given by

$$\frac{d\Omega_\phi}{dt} = -\frac{\Omega_\phi}{\tau_{\Omega_\phi}} + \frac{1}{m_p R_0^2}\left(\sum_{i=1}^{N_{NBI}} k_{NBI,i} P_{NBI,i} + k_{int}\frac{W}{I_p}\right) + \delta_{\Omega_\phi}, \tag{9}$$

where $\tau_{\Omega_\phi} \triangleq k_{\Omega_\phi}\tau_E$ is the characteristic time of the Ω_ϕ dynamics, k_{Ω_ϕ} is a model constant, τ_E is modeled by (8), m_p is the total plasma mass, $k_{NBI,i}$ are model parameters for the torque deposition of the i-th NBI, k_{int} is a model parameter for the intrinsic-torque effects [27], and δ_{Ω_ϕ} is a model uncertainty that characterizes other unmodeled sources of torque within the plasma, and for which a bound can be estimated.

3.4. Magnetic Island-Width Dynamics

The dynamic evolution of the magnetic island-width, w (depicted in Fig. 2), is modeled by the modified Rutherford equation. For consistency with the NTM-suppression controllers developed in previous work, the version utilized in this work is derived from that in [21] (see Appendix C for details),

$$\begin{aligned}\frac{\tau_R}{r}\frac{dw}{dt} &= \Delta_0' r + a_2\frac{j_{BS}(\hat{\rho}_{NTM})}{j_\phi(\hat{\rho}_{NTM})}\frac{L_q}{w}\left(1 - \frac{w_{marg}^2}{3w^2}\right) \\ &\quad - \frac{a_2 L_q}{j_\phi(\hat{\rho}_{NTM})}\left[\sum_{k=1}^{k=N_{EC,pre}}\left(F_{pre,k}^* + \frac{K_{pre,k}}{w}\right) j_{pre,k}^{max} + \left(F_{act}^* + \frac{K_{act}}{w}\right) j_{act}^{max}\right],\end{aligned} \tag{10}$$

where τ_R is the island's resistive diffusion time, r is the radial location of the island (see Fig. 2), Δ_0' is the classical tearing stability index (approximated as $\Delta_0' r \approx -m$ for a mode at $q = m/n$), a_2 is a geometric factor, j_{BS} is the bootstrap current density, j_ϕ is the toroidal current density, $\hat{\rho}_{NTM}$ is the location of the island's O-point expressed in terms of $\hat{\rho}$, $L_q \triangleq (q/|dq/dr|)\,|_{\hat{\rho}_{NTM}}$ is the local magnetic-shear length, and w_{marg} is the marginal island-width. The third term on the right-hand side of (10) models how w is affected by the pre-emptive [21] EC launchers (where the summation is done for $k = 1, ..., N_{EC,pre}$, and $N_{EC,pre}$ is the total number of pre-emptive EC launchers) and active-suppression EC group [20], so $j_{pre,k}^{max}$ is the maximum current-density driven by the

k-th pre-emptive launcher, j_{act}^{max} is the maximum current-density driven by the active-suppression group, and $K_{pre,k}$, $F^*_{pre,k}$, K_{act}, and F^*_{act} are functions that depend on the ECH&CD alignment with the magnetic island O-point [21].

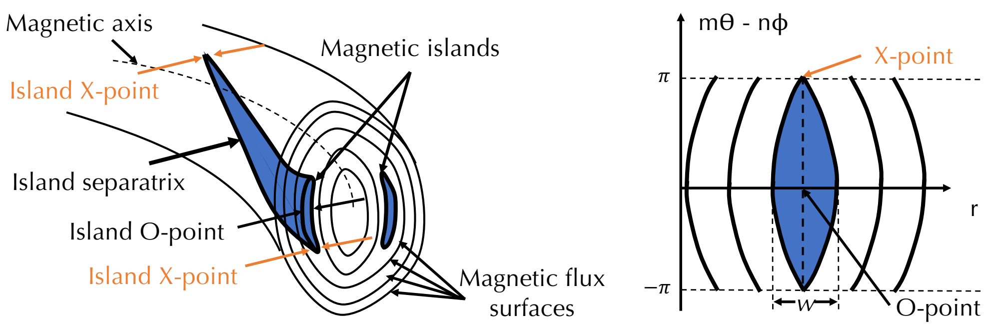

Figure 2: Schematic of the magnetic-island geometry for a mode with poloidal and toroidal mode numbers m and n, respectively. In this figure, the variables θ and ϕ denote the poloidal and toroidal mode angles, respectively.

To close the model, the island's resistive diffusion time is modeled as $\tau_R = \frac{\mu_0 \pi r w}{1.22\,\eta(\hat{\rho}_{NTM})}$ [21], whereas the marginal-island width is estimated as $w_{marg} = 2\sqrt{\epsilon}\rho_{i,\theta}$, where $\rho_{i,\theta} = 2.043 \times 10^{-4}\sqrt{T_D(\hat{\rho}_{NTM})/B_\theta(\hat{\rho}_{NTM})}$, T_D is the temperature of the deuterium ions, and B_θ is the poloidal magnetic field. A tight coupling between deuterium-ion and electron temperatures is assumed in this control-synthesis model as given by $T_D \approx 2T_e^{prof} I_p \sqrt{P_{tot}}\bar{n}_e^{-1}$, where T_e^{prof} is a model profile. It is considered that j_ϕ, $\hat{\rho}_{NTM}$, L_q, and B_θ are available in real time because they can be calculated from a real-time estimation of the q profile (see, for example, [28]). However, although q_0 and q_e control is considered in this work, complete regulation of the whole q profile is not ensured. Therefore, the values of j_ϕ, $\hat{\rho}_{NTM}$, L_q, and B_θ derived from q are treated as inputs to the system that are not directly controlled.

3.5. Control-Synthesis Model Summary and Individual-Scalar Control Goal

The control-synthesis model described in Sections 3.1 through 3.4 is summarized as

$$\frac{d}{dt}\begin{bmatrix} q_0 \\ q_e \\ W \\ \Omega_\phi \\ w \end{bmatrix} = \begin{bmatrix} f_{q_0}(q_0, I_p, P_{NBI,i}, P_{EC,j}, \hat{\rho}_{EC,j}, \bar{n}_e, \delta_{q_0}) \\ f_{q_e}(q_e, I_p, \delta_{q_e}) \\ f_W(W, I_p, P_{NBI,i}, P_{EC,j}, \bar{n}_e, \delta_W) \\ f_{\Omega_\phi}(\Omega_\phi, W, I_p, P_{NBI,i}, P_{EC,j}, \bar{n}_e, \delta_{\Omega_\phi}) \\ f_w(w, I_p, P_{NBI,i}, P_{EC,j}, \hat{\rho}_{EC,j}, q, \bar{n}_e) \end{bmatrix}, \tag{11}$$

or equivalently,

$$\frac{dx}{dt} = f(x, u, \delta, t), \tag{12}$$

where the state vector is given by $x = [q_0, q_e, W, \Omega_\phi, w]^T$, the controllable-input vector is given by $u = [I_p, P_{NBI,1}, ..., P_{NBI,N_{NBI}}, P_{EC,1}, ..., P_{EC,N_{EC}}, \hat{\rho}_{EC,1}, ..., \hat{\rho}_{EC,N_{EC}}]^T$, $\delta = [\delta_{q_0}, \delta_{q_e}, \delta_W, \delta_{\Omega_\phi}]^T$ is the vector of uncertainties, and $f = [f_{q_0}, f_{q_e}, f_W, f_{\Omega_\phi}, f_w]^T$, where the functions f_{q_0}, f_{q_e}, f_W, f_{Ω_ϕ}, and f_w are given by the right-hand sides of (3), (6), (7), (9), and (10), respectively. The dependence of the state function f with t in (12) is due to the inputs $\bar{n}_e$ and q.

For each state-vector component, denoted by x_k ($k = 1, ..., 5$), the control goal of the associated controller is to regulate x_k around a target $\bar{x}_k$ for all values $\delta_k \in [-\delta_k^{max}, \delta_k^{max}]$ (where δ_k^{max} is the bound for the uncertainty δ_k associated with x_k) by means of u, where $u \in [u_{min}, u_{max}]$, and u_{min} and u_{max} are the minimum and maximum saturation limits for u, respectively. It can be noted that the magnetic island-width subsystem described by f_w, equation (10), does not include any uncertainty, so $\delta_5 \equiv 0$.

4. Components of the Integrated-Control Architecture

4.1. Individual-Scalar Controllers

4.1.1. Kinetic and Magnetic Scalar Controllers

These controllers calculate the required values of j_{q_0}, I_p, P_{tot}, and T_{NBI} (denoted as $j_{q_0}^{req}$, I_p^{req}, P_{tot}^{req}, and T_{NBI}^{req}, respectively) to regulate q_0, q_e, W, and Ω_ϕ, respectively. To simplify the presentation of these controllers in this section, a generic derivation is used with x_k, δ_k, and f_k (which denotes each of the components of f), for $k = 1, ..., 4$. The high-level actuation requests are denoted as $j_{q_0}^{req} \triangleq U_1^{req}$, $I_p^{req} \triangleq U_2^{req}$, $P_{tot}^{req} \triangleq U_3^{req}$, and $T_{NBI}^{req} \triangleq U_4^{req}$, and generically as U_k^{req}. For real-time calculation purposes, it is assumed that an estimation of x_k is available (as is the case in DIII-D [28]).

The control synthesis of each controller has two steps. In the first step, a nominal controller is synthesized with $\delta_k \equiv 0$. Setting the right-hand side of f_k as

$$f_k(x_k, U_k^{nom,req}, 0, t) \triangleq -K_P^k \tilde{x}_k - K_I^k \int_{t_0}^{t_l} \tilde{x}_k dt + \frac{d\bar{x}_k}{dt}, \tag{13}$$

where $U_k^{nom,req}$ is the nominal controllable input, $\tilde{x}_k \triangleq x_k - \bar{x}_k$ is the error variable associated with x_k, t_0 is the time when the feedback-control for x_k is turned on, and $K_P^k > 0$ and $K_I^k > 0$ are the proportional and integral gain, respectively. Using (13), the nominal W dynamics becomes

$$\frac{d\tilde{x}_k}{dt} = -K_P^k \tilde{x}_k - K_I^W \int_{t_0}^{t_l} \tilde{x}_k dt, \tag{14}$$

which is an exponentially stable system, i.e. the error dynamics for x_k can be bounded as $|\tilde{x}_k| \leq k_1 e^{-k_2(t-t_0)}$, for some constants $k_1 > 0$ and $k_2 > 0$. This can be shown by solving (14) directly, or by using Lyapunov theory (see Appendix D). Therefore, $\tilde{x}_k \to 0$ when $t \to \infty$ as long as $\delta_k \equiv 0$ under the nominal feedback-control law (13), or what is the same, x_k tends to $\bar{x}_k$, achieving the desired control goal.

However, in the general case when $\delta_k \neq 0$, exponential stability of the x_k uncertain dynamics cannot be ensured. In the second step of the control synthesis, Lyapunov redesign techniques are employed [29] to overcome this limitation. The uncertain x_k

dynamics with $U_k^{req} \triangleq U_{tot}^{nom,req} + U_{tot}^{rob,req}$, where $U_{tot}^{rob,req}$ is a term that needs to be designed to ensure robustness, is given by

$$\frac{d\tilde{x}_k}{dt} = -K_P^k \tilde{W} - K_I^k \int_{t_0}^{t_l} \tilde{x}_k dt + f_\delta^k U_{tot}^{rob} + \delta_k, \tag{15}$$

where $f_\delta^k = 1$ (for $k = 1$ and $k = 3$), $f_\delta^2 = -k_{I_p}^{nom}/\Delta_t$ (where Δ_t is the controller sampling time), and $f_\delta^4 = 1/(m_p R_0^2)$. Using a Lyapunov function $V_k = \frac{1}{2}\tilde{x}_k^2 + \frac{1}{2}K_I^k \left(\int_{t_0}^{t_l} \tilde{x}_k dt\right)^2$, and taking the time derivative, it is found that

$$\frac{dV_k}{dt} = -K_P^k \tilde{W}^2 + \tilde{x}_k \left(\delta_k + f_\delta^k U_k^{rob,req}\right). \tag{16}$$

Setting $U_k^{rob,req}$ as

$$U_k^{rob,req} \triangleq -\frac{\delta_k^{max}}{f_\delta^k}\,\mathrm{sign}(\tilde{x}_k), \text{ if } |\tilde{x}_k| \geq \epsilon_k, \quad U_k^{rob,req} \triangleq -\frac{(\delta_k^{max})^2}{f_\delta^k}\frac{\tilde{x}_k}{\epsilon_k}, \text{ if } |\tilde{x}_k| < \epsilon_k, \tag{17}$$

where ϵ_k is a design parameter that is chosen such that $0 < \epsilon_k < |\tilde{x}_k(t_0)|$, and $|\delta_k| \leq \delta_k^{max}$, then $\frac{dV_k}{dt}$ can be bounded as

$$\frac{dV_k}{dt} \leq -K_P^k \tilde{x}_k^2 + f_\delta^k \delta_k^{max} \left(|\tilde{x}_k| - \tilde{x}_k \mathrm{sign}(\tilde{x}_k)\right) \leq -K_P^k \tilde{x}_k^2, \quad \text{if } |\tilde{x}_k| \geq \epsilon_k, \tag{18}$$

or alternatively, as

$$\frac{dV_k}{dt} \leq -K_P^k \tilde{W}^2 + f_\delta^k \delta_k^{max} |\tilde{x}_k| - \frac{(\delta_k^{max})^2 \tilde{x}_k^2}{\epsilon_k} \leq -K_P^k \tilde{x}_k^2 + \frac{\epsilon_k}{4}, \quad \text{if } |\tilde{x}_k| < \epsilon_k, \tag{19}$$

where it has been used that $f_k^* \triangleq \delta_k^{max}|\tilde{x}_k| - \frac{(\delta_k^{max})^2 \tilde{x}_k^2}{\epsilon_k}$ has an absolute maximum at $\delta_k^{max}|\tilde{x}_k| = \frac{\epsilon_k}{2}$ at which $f_k^*(\frac{\epsilon_k}{2}) = \frac{\epsilon_k}{4}$. Therefore, it can be concluded that $|\tilde{x}_k| \leq \epsilon_k$ after a transient period during which $\tilde{x}_k$ is also bounded (see Appendix E, in which μ plays the role of ϵ_k). Also, in order to have an error $\tilde{x}_k$ that is as close to zero as possible (i.e. in order to have $x_k \to \bar{x}_k$), ϵ_k must be taken very small, $\epsilon_k \to 0$.

The high-level actuation requests calculated by the controllers described in this section, i.e. $U_1^{req} = U_1^{req,nom} + U_1^{req,rob} = j_{q0}^{req}$, $U_2^{req} = U_2^{req,nom} + U_2^{req,rob} = I_p^{req}$, $U_3^{req} = U_3^{req,nom} + U_3^{req,rob} = P_{tot}^{req}$, $U_4^{req} = U_4^{req,nom} + U_4^{req,rob} = T_{NBI}^{req}$, are then sent to the actuator manager (see Section 4.4).

In addition, constant values of the ECCD radial location, $\hat{\rho}_{EC,j}^{req}$, are set for individual-scalar control. Such ECH&CD aiming is determined in an off-line fashion with the purpose of maximizing the performance of the applicable plasma [30]. The values of $\hat{\rho}_{EC,j}^{req}$ are sent as actuation requests to the actuator manager (see Section 4.4).

4.1.2. NTM Suppression by means of $P_{EC,j}$

The high-level actuation requests calculated by this controller are the EC powers, $P_{EC,j}^{req}$, composed of the active-suppression power, P_{act}^{req}, and the pre-emptive powers, $P_{pre,k}^{req}$ (k = 1, ..., $N_{EC,pre}$). It is considered that $P_{pre,k}^{req}$ are fixed and set equal to the maximum available power. Also, $\hat{\rho}_{EC,j}$ are determined separately by the NTM-suppression controllers in Section 4.2. As a result, the only variable left for real-time control is P_{act}^{req}, for which a controller is designed using Lyapunov theory [29]. For calculation purposes within this controller, it is assumed that real-time estimations for w and q exist.

The w dynamics, equation (10), is considered. By setting

$$j_{act}^{max} = \frac{K_P^w \frac{w^2 \tau_R j_\phi}{r L_q} + j_{BS}}{w F_{act}^* + K_{act}}, \tag{20}$$

within (10), where $K_P^w > 0$ is a design parameter, then (10) becomes

$$\frac{\tau_R}{r}\frac{dw}{dt} = \Delta_0' r - \frac{\tau_R}{r} a_2 K_P^w w - a_2 \frac{j_{BS}}{j_\phi}\frac{L_q}{w}\frac{w_{marg}^2}{3w^2} - \frac{a_2 L_q}{j_\phi}\sum_k \left(F_{pre,k}^* + \frac{K_{pre,k}}{w}\right) j_{pre,k}^{max}. \tag{21}$$

It is assumed that the pre-emptive action through $P_{pre,k}^{req}$ provides a stabilizing effect, so the last term in (21) is non-positive. Because the first and third terms on the right-hand side of (21) are always strictly negative for NTMs, dw/dt in (21) can be bounded as $\frac{dw}{dt} < -a_2 K_P^w w$, i.e. $w < w_0 e^{-t/\tau}$, where w_0 is the initial island width, and $\tau \triangleq 1/(a_2 K_P^w)$. Therefore, (21) is an exponentially stable system [29]. Setting j_{act}^{max} as in (20) ensures that $w \to 0$ as $t \to \infty$ bounded by an exponential with characteristic time τ. The required power for active suppression, P_{act}^{req}, is computed from (20) together with the model for ECH&CD (see (A.3) in Appendix A and/or [31]) and the decomposition into pre-emptive and active-suppression EC launchers (see Section 3.4 and (C.3) in Appendix C), as given by

$$P_{act}^{req} = \frac{1}{j_{act}^{dep}(\hat{\rho}_{act}^{max})}\left[\frac{n_e(\hat{\rho}_{act}^{max})}{T_e(\hat{\rho}_{act}^{max})}\frac{\frac{\tau_R}{r}\frac{K_P^w j_\phi}{L_q} w^2 + j_{BS}}{w F_{act}^* + K_{act}} - \sum_k j_{pre,k}^{max} P_{pre,k}^{req}\right], \tag{22}$$

where $\hat{\rho}_{act}^{max}$ is the location of the maximum active-suppression EC current-deposition. It must be noted that, if uncertainties were present within (21) (e.g. to model the influence of complex physics such as rotation-shear stabilization effects or others), Lyapunov redesign could be used, similarly as in Section 4.1.1, to design a less conservative estimate of P_{act}^{req} compared to that obtained in (22). Moreover, a similar approach could be followed to design a controller that is robust against a potential misalignment between the ECCD aiming and the island O-point.

4.2. NTM Suppression by means of $\hat{\rho}_{EC,j}$

The high-level actuation requests calculated by these controllers are the required ECCD radial location (denoted by $\hat{\rho}_{pre,k}^{req}$ and $\hat{\rho}_{act}^{req}$ for pre-emptive and active suppression, respectively). Control algorithms that steer the mirror-aiming location for NTM suppression have been previously designed and tested in DIII-D [20, 21], which allow for modifying the ECCD radial location. This previous work employed two main techniques: pre-emptive stabilization and active suppression. With pre-emptive stabilization, the corresponding EC powers (i.e. $P_{pre,k}$) are always on and applied at particular $q = m/n$ rational surfaces that are prone to NTMs, so that magnetic islands do not develop. For the aiming, $\hat{\rho}_{pre,k}^{req}$ are determined in real time to point at such moving rational surfaces, even if a mode has not developed. On the other hand, with active-suppression techniques, the EC power (i.e. P_{act}) remains off until an NTM is detected. Then, P_{act} is turned on, and $\hat{\rho}_{act}^{req}$ is steered toward the spatial location of the magnetic island O-point. If sufficient shrinkage of the magnetic island is achieved with active suppression, the EC power is turned back off. It must be noted that, in general, the values of $\hat{\rho}_{act}^{req}$ and $\hat{\rho}_{pre,k}^{req}$ are different, as the rational surfaces that a priori are prone to NTMs may not be the ones actually developing them. Details regarding modeling, control synthesis, and implementation of these NTM-suppression controllers can be found in [20, 21].

4.3. Supervision and Exception Handling: Off-Normal and Fault-Response System, Off-Line Control Priorities

Supervisory and exception handling (S&EH) systems will be a critical component in future integrated PCSs. In general terms, a S&EH system receives information from the plasma state in order to decide, in real time, the priorities of the control tasks that need to be carried out for a safe and efficient tokamak operation.

The Off-Normal and Fault-Response (ONFR) system [15], implemented and tested within the DIII-D PCS, has some S&EH capabilities. It has the capability of monitoring MHD instabilities like Tearing Modes (TMs) with a particular n mode number, as well as other off-normal events such as locked modes, disruptions, high plasma density, or high radiated power. With this information of the plasma state, ONFR calculates the necessary control priorities for a safe plasma operation. In this work, the ONFR system has been employed during DIII-D experiments to monitor the NTM development so that, in conjunction with the individual-scalars controllers, NTM-suppression controllers, and AM algorithm, simultaneous control objectives can be attained. The ONFR system determines the NTM-suppression control priority based on the n mode amplitude. When this amplitude is above a particular “detection” threshold, the control priority for NTM suppression is activated. When the amplitude is below a certain “recovery” threshold (i.e. if the mode is suppressed), the control priority for NTM suppression is removed.

In addition to the MHD-monitoring carried out by ONFR, the control priorities for the other control tasks are defined in an off-line fashion. These off-line priorities determine the relative importance of the individual-scalar control tasks. As an example, there may be periods of time when W control should be prioritized over Ω_ϕ control, and/or discharge phases when q_e and q_0 control may have the same importance for a particular scenario.

Both the ONFR-determined and off-line priorities compose the control priorities that the AM receives. These priorities may switch in real time. For instance, when an NTM that needs suppression is detected, the NTM-suppression control priority is sent to the AM so that the NTM-suppression actuation requests are fulfilled as closely as possible. Control of the individual scalars would also be attempted simultaneously, if possible, according to the relative importance set by the off-line priorities. On the other hand, when there is no need for NTM suppression, the NTM-suppression control priority is not activated. Real-time changes to the control priorities are accounted by means of the design matrices embedded in the AM algorithm (see Section 4.4).

4.4. Actuator Manager based on Nonlinear, Real-Time Optimization

Within the PCS architecture proposed in this work, numerous kinetic, magnetic, and MHD control tasks need to be carried out, sometimes simultaneously, by a finite number of actuators. Examples include the ECH&CD sharing for NTM suppression, W, and q_0 control purposes, or the NBI sharing for W and Ω_ϕ regulation. The goal of the AM algorithm is calculating, in real time, the controllable-input vector $u = [I_p, P_{NBI,1}, ..., P_{NBI,N_{NBI}}, P_{EC,1}, ..., P_{EC,N_{EC}}, \hat{\rho}_{EC,1}, ..., \hat{\rho}_{EC,N_{EC}}]^T$ that fulfills as many control objectives (i.e., actuation requests) as possible, while also considering actuator limits and availability, as well as other secondary objectives when possible (e.g., minimizing the overall control effort). The AM algorithm is based on real-time optimization [22]. It receives three main types of information:

- The actuation requests from individual-scalar and NTM-suppression controllers, namely, P_{tot}^{req}, T_{NBI}^{req}, I_p^{req}, $j_{q_0}^{req}$, $P_{EC,j}^{req}$ (i.e. P_{act}^{req} and $P_{pre,k}^{req}$), $\hat{\rho}_{EC,j}^{req}$, $\hat{\rho}_{act}^{req}$, and $\hat{\rho}_{pre,k}^{req}$.
- Physical saturation limits from the actuator systems.
- Control priorities and scenario/actuator parameters from S&EH systems.

The optimization problem that is solved in real time is given by

$$\min_{u,s} u^T R u + s^T Q s, \text{ subject to} \tag{23}$$

Kinetic control constraints:

$$\sum_{i=1}^{i=N_{NBI}} P_{NBI,i} + \sum_{j=1}^{j=N_{EC}} P_{EC,j} = P_{tot}^{req} + s_{P_{tot}}, \tag{24}$$

$$\sum_{i=1}^{i=N_{NBI}} k_{NBI,i} P_{NBI,i} = T_{NBI}^{req} + s_{T_{NBI}}, \tag{25}$$

Magnetic control constraints:

$$I_p = I_p^{req} + s_{I_p}, \tag{26}$$

$$j_{q_0}(q_0, I_p, P_{NBI,i}, P_{EC,j}, \hat{\rho}_{EC,j}) = j_{q_0}^{req} + s_{j_{q_0}}, \tag{27}$$

$$\hat{\rho}_{EC,1} = \hat{\rho}_{EC,1}^{req} + s_{\hat{\rho}_{EC,1}}, \tag{28}$$

$$\vdots$$

$$\hat{\rho}_{EC,N_{EC}} = \hat{\rho}_{EC,N_{EC}}^{req} + s_{\hat{\rho}_{EC,N_{EC}}}, \tag{29}$$

NTM suppression constraints:

$$P_{EC,1} = P_{EC,1}^{req} + s_{P_{EC,1}}, \tag{30}$$

$$\vdots$$

$$P_{EC,N_{EC}} = P_{EC,N_{EC}}^{req} + s_{P_{EC,N_{EC}}} \tag{31}$$

$$\text{either } \hat{\rho}_{EC,1} = \hat{\rho}_{pre,1}^{req} + s_{\hat{\rho}_{EC,1}}, \tag{32}$$

$$\text{or } \quad \hat{\rho}_{EC,1} = \hat{\rho}_{act,1}^{req} + s_{\hat{\rho}_{EC,1}}, \tag{33}$$

$$\vdots$$

$$\text{either } \hat{\rho}_{EC,N_{EC}} = \hat{\rho}^{req}_{pre,N_{EC}} + s_{\hat{\rho}_{EC,N_{EC}}}, \tag{34}$$

$$\text{or} \quad \hat{\rho}_{EC,N_{EC}} = \hat{\rho}^{req}_{act,N_{EC}} + s_{\hat{\rho}_{EC,N_{EC}}}, \tag{35}$$

Physical saturation limits: $$u \in [u_{min}, u_{max}], \tag{36}$$

where $s = [s_{P_{tot}}, s_{T_{NBI}}, s_{I_p}, s_{j_{q0}}, s_{P_{EC,1}}, ..., s_{P_{EC,N_{EC}}}, s_{\hat{\rho}_{EC,1}}, ..., s_{\hat{\rho}_{EC,N_{EC}}}]^T$ is a vector of slack variables that characterize the fulfillment of a particular actuation request, and Q and R are design matrices that determine how the different control tasks and actuators are prioritized.

The concrete meaning of s, Q, and R is explained next. Each component of s represents a lack or excess in the realization of the related high-level actuation request. Such lack or excess may be found when reaching saturation limits (e.g. if P^{req}_{tot} is so high that all actuators saturate to their upper values, then $s_{P_{tot}} < 0$ will be found - for instance, if the W controller request is 10 MW but only 8 MW are available, $s_{P_{tot}} = -2$ MW) or due to prioritization conflicts with other control tasks (e.g. if very accurate Ω_ϕ control is requested that cannot be carried out simultaneously with W control, then $s_{P_{tot}} \neq 0$, or if both W and Ω_ϕ control have the same priority but cannot be carried out simultaneously, then $s_{P_{tot}} \neq 0$ and $s_{\Omega_\phi} \neq 0$). The matrix Q has the capability of prioritizing one or more control tasks against others because it determines how large the components of s can get. For example, if NTM suppression is needed as determined by the S&EH system, then the terms in Q related to $s_{P_{EC,j}}$ and $s_{\hat{\rho}_{EC,j}}$ will be much higher in order to make those slack quantities small and prioritize the use of ECH&CD for this control task. On the other hand, the matrix R has the capability of prioritizing the use of certain actuators against others. If an actuator's control action becomes "expensive" (for instance, as a protective measure for excessive power-modulation of an NBI), the terms in R related to the particular actuator will be increased (in order to use less of power from that particular NBI). Thus, the AM algorithm finds the optimal actuator requests u that minimize s while respecting the control-task and actuator prioritization.

It must be noted that the AM algorithm described in (23)-(36) allows for carrying out the two main types of actuator sharing envisioned for ITER [3]: simultaneous multiple-mission sharing (a continuous sharing of actuator(s) for more than one control task) and repurposing sharing (a fast repurpose of actuator(s) from one control task to another, usually as a result of an off-normal event).

5. Simulation Testing of the Integrated Architecture using COTSIM

5.1. Plasma Models for Simulation

The control architecture has been tested in simulations using COTSIM, a control-oriented code developed by the Plasma Control Group at Lehigh University. Within this 1D simulation code, different equations are employed to simulate the current, heating, momentum, and particle transport dynamics, as well as the magnetic-island width, pedestal, and equilibrium evolutions.

For the plasma magnetic diffusion, a version of the magnetic-diffusion equation similar to that in Appendix A is implemented, but generalized to use a 2D time-varying equilibrium and other types of auxiliary sources like lower-hybrid or ion-cyclotron heating. For the core T_e (the pedestal model is introduced later), an electron heat-transport equation is implemented,

$$\frac{3}{2}\frac{\partial\left(n_e T_e\right)}{\partial t}=\frac{1}{\rho_b^2\hat{H}\hat{\rho}}\left(\frac{\hat{G}\hat{H}^2}{\hat{F}}\chi_e n_e\frac{\partial T_e}{\partial\hat{\rho}}\right)+Q_e, \tag{37}$$

where χ_e is the electron thermal diffusivity, and Q_e is the electron-heat deposition from different sources, as ohmic, radiation, and electron-ion collision heating. For χ_e, a number of analytical models are available for both neoclassical and anomalous transport, including the Chang-Hinton neoclassical model [24], a mixed Bohm/gyro-Bohm model [32], or the Coppi-Tang model [33]. Analytical, physics-based models are employed to estimate the pedestal evolution [34],

$$T_e^{ped}=\frac{\Delta}{2n_e^{ped}\frac{\alpha_c B_T^2}{2\mu_0 R^{ped}{q^{ped}}^2}},\quad \alpha_c=0.8s^{ped}\frac{1+\kappa_{95}^2(1+5\delta_{95}^2)}{2}, \tag{38}$$

where Δ is the pedestal width, α_c is the maximum normalized pressure-gradient, T_e^{ped}, R^{ped}, q^{ped}, n_e^{ped}, and s^{ped} are pedestal-top values for T_e, major radius R, q, n_e, and magnetic shear $s\triangleq\frac{r}{q}\frac{dq}{dr}$, respectively, and κ_{95} and δ_{95} are the elongation and triangularity, respectively, of the flux surface that encloses 95% of the total toroidal flux. For the toroidal rotation profile, ω_ϕ, a momentum-transport equation adapted from [35] is employed,

$$m_i\langle r^2\rangle\frac{\partial\left(n_i\omega_\phi\right)}{\partial t}=\frac{1}{\hat{\rho}\hat{H}}\frac{\partial}{\partial\hat{\rho}}\left(\hat{\rho}n_i m_i\hat{H}\langle r^2(\nabla\hat{\rho})^2\rangle\chi_\phi\frac{\partial\omega_\phi}{\partial\hat{\rho}}\right)+t_\omega, \tag{39}$$

where m_i is the ion mass, n_i is the ion density, χ_ϕ is the ion momentum diffusivity, $\langle r^2\rangle$ and $\langle r^2(\nabla\hat{\rho})^2\rangle$ are geometric factors of the plasma equilibrium, and t_ω is the ion-torque deposition from different sources. For χ_ϕ, the approximation $\chi_\phi\approx f_\phi(\hat{\rho})\chi_e$ is employed, where f_ϕ is a model profile. For t_ω, control-oriented models are employed that consider several types of contributions, such as the NBI, 3D-coil, and intrinsic torques. A version of the modified Rutherford equation similar to (10) is also implemented to estimate the dynamics of w. Such equation is coupled with the rest of the transport equations in COTSIM, so that the development of NTMs decreases the overall confinement levels as modeled by a modified electron thermal diffusivity, χ_e^{mod}, that substitutes χ_e when $w>0$. The model for χ_e^{mod} is given by

$$\chi_e^{mod}=\chi_e+f_{NTM}(\hat{\rho},w),\quad f_{NTM}=C_{NTM,1}\exp\left[-C_{NTM,2}\left(\frac{\hat{\rho}-\hat{\rho}_{NTM}}{w}\right)^2\right], \tag{40}$$

where $C_{NTM,1}$ and $C_{NTM,2}$ are constant parameters. Finally, a 2D analytical equilibrium-solver [36] is employed to estimate the time evolution of the plasma equilibrium, so the geometric factors within the transport equations are updated at every time step.

The simulation models presented in this section include more comprehensive plasma-dynamics than the control-synthesis models described in Section 3. It must be noted that, although several simplifying assumptions are still made, the increase in model complexity represents a challenging test during simulations for the controllers' robustness against unknown dynamics. Due to the modular nature of COTSIM, the physics complexity of the source, transport, and equilibrium models can be increased if needed. For instance, a different model for χ_e could be adopted to characterize the confinement variations due to MHD activity, a different equilibrium reconstruction method could be employed, or a more realistic model for χ_ϕ could be utilized.

5.2. Simulation Study in DIII-D Steady-State Scenario

The objective of this simulation study is to assess the control scheme's performance to regulate the individual scalars when NTMs are present in the DIII-D high-q_{min} scenario, which is one of the candidate scenarios for steady-state operation in ITER [25]. In particular, the plasma parameters in these simulations are within a range similar to those in shot 172538 (i.e. $I_p \approx 1.05$ MA, $B_T \approx 1.65$ T, $\beta_N \approx 3.5$, $\bar{n}_e \approx 4.5 \times 10^{19}$ m^{-3}, and relatively high non-inductive current fraction ($\approx 75\%$) [25]). In accordance with the NBI systems available in DIII-D, three NBI groups are used in simulation, namely, on-axis co-current NBIs, off-axis co-current NBIs, and counter-current NBIs. Their powers are denoted by P_{NBI}^{ON} (the sum of the powers of the co-current NBIs with on-axis deposition, which are located at toroidal angles of 30 deg and 330 deg in DIII-D), P_{NBI}^{150} (co-current beamline with off-axis deposition located at toroidal angle of 150 deg in DIII-D), and P_{NBI}^{210} (counter-current beamline located at toroidal angle of 210 deg in DIII-D), respectively. Also, three ECH&CD launchers are employed ($N_{EC} = 3$) whose poloidal mirrors can be controlled independently. At the beginning of the shot, ECH&CD is set up to carry out individual-scalar control. Due to the relatively low number of ECH&CD launchers, both active suppression and pre-emptive suppression employ all three available ECH&CD launchers in this simulation. Therefore, when active suppression is used, $N_{EC,pre} = 0$ is adopted (i.e. all launchers are used within the active-suppression group and without pre-emptive dedicated launchers), whereas if pre-emptive suppression is used, $N_{EC,pre} = 3$ is adopted.

Several simulations are executed in this study. First, a feedforward (FF) simulation is run with the experimental inputs from shot 172538, except for the total EC power, $P_{EC} \triangleq \sum P_{EC,j}$, which is limited from 3.5 MW to 1.5 MW. Also, the development of a 2/1 NTM is emulated after $t = 2.7$ s as a result of the reduced P_{EC}, thus simulating an H-mode plasma with relatively low performance. Only feedforward inputs are employed in this first simulation, i.e. no feedback (FB) is employed. For clarity, this simulation is referred to as "FF only" both in the text and figures of this section. Second, another FF simulation is run with lower I_p (-0.05 MA compared to 172538), $P_{EC} \approx 1.5$ MW after $t \geq 2.4$ s, increased P_{NBI}^{150} (+25% with respect to 172538) and decreased P_{NBI}^{ON} (-25% with respect to 172538). No NTM is emulated in this case. This second simulation would correspond to a trophy plasma with relatively higher performance. For clarity, it is referred to as "target" both in the text and figures of this section. Therefore, the evolutions for the scalars during this second simulation are set as targets, i.e., $\bar{x} = [\bar{q}_0, \bar{q}_e, \bar{W}, \bar{\Omega}_\phi, 0]^T$. Finally, a third simulation is executed in which the FF + FB control scheme is turned on at $t = 0.9$ s. The goal in this FF + FB simulation is to show that, by means of FB, the scalar evolutions can be driven from the "FF-only" case to the "target" case, i.e the goal is driving x toward $\bar{x}$. It must be kept in mind that the FF+FB controllers use the FF inputs from the first simulation (i.e. the FF-only simulation), but they do not have any knowledge about the inputs associated with the second simulation (target). Under FB, the NTM-suppression controller is activated at $t = 2.7$ s. Later, when $t \geq 5$ s, an off-line control priority is set up at $t \geq 5$ s to stop doing any kind of NTM suppression, with the goal of illustrating the capabilities of the control scheme. Also, in order to make the simulation testing more realistic, noise levels with frequencies between 40 and 60 Hz are added to the estimations of W, Ω_ϕ, q_0, and q_e employed for FB control. In order to deal with such noise, the FB controllers are equipped with low-pass filters with a cutoff frequency of 40 Hz, so that most of the measurement noise is filtered without making the control response too slow.

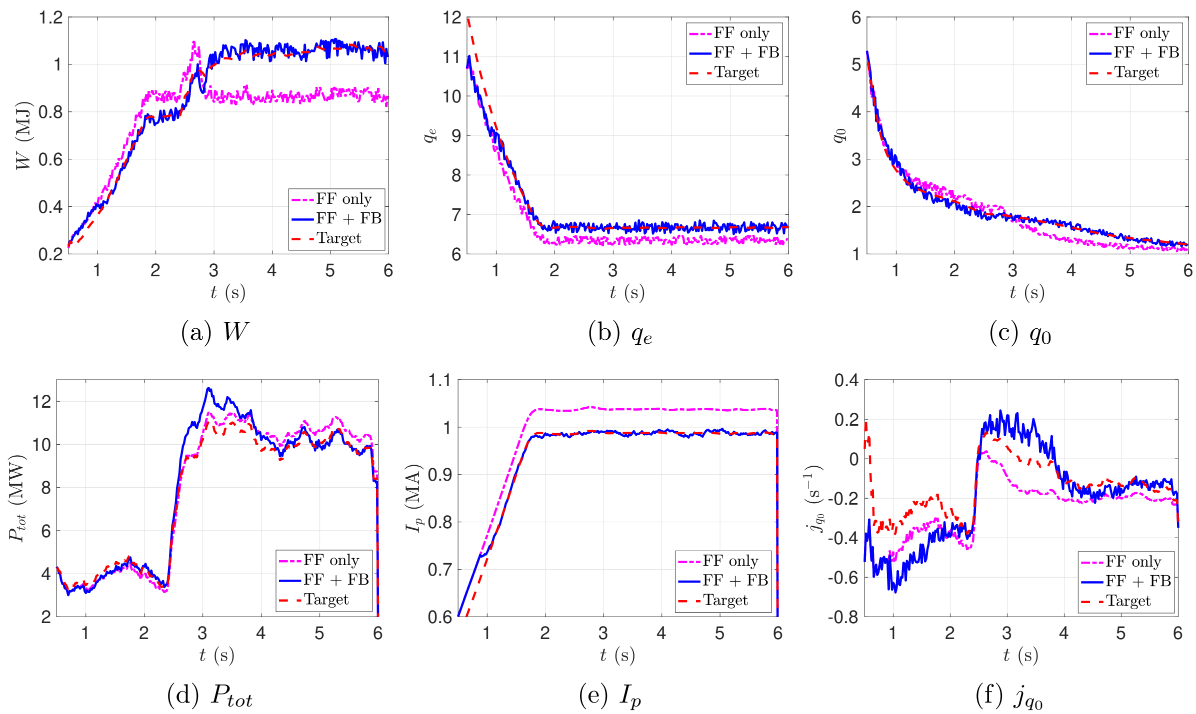

(a) W (b) q_e (c) q_0

(d) P_{tot} (e) I_p (f) j_{q_0}

Figure 3: Time evolutions for W, q_e, q_0, P_{tot}, I_p, and j_{q_0} in FF-only (magenta dashed-dotted) and FF + FB (blue solid) during simulations using COTSIM, together with the targets (red dashed).

Fig. 3 shows the evolution of W, q_e, and q_0, together with their respective high-level actuation requests from the individual-scalar controllers, P_{tot}, I_p, and j_{q_0}. It can be seen that, up until $t = 0.9$ s, the FF-only and FF + FB simulations are very similar (the small differences are caused by the measurement noise). In the FF + FB simulation, right after the FB is turned on, W is decreased toward its target $\bar{W}$ (see Fig. 3a) by modulating P_{tot} (see Fig. 3d) until W gradually reaches its target value. At $t = 2.7$ s, a drop in W can be appreciated in both the FF-only and FF + FB cases due to NTM development. In the FF-only case, W drops and stays well below the target due to the confinement deterioration caused by the MHD activity. In the FF + FB case, however, W recovers and tracks its target. Although W is driven toward its target quite fast (in about 0.5 s) under FB, the confinement deterioration suffered by the plasma makes P_{tot} drift toward the associated target evolution more slowly. An increase in the overall FF + FB value of P_{tot} can be observed for about a second after the appearance of the NTM. Later in the simulation ($t \geq 4.25$ s), the P_{tot} evolution in FF + FB converges towards its target value, which is in fact lower than the FF-only value. In addition, q_e is successfully regulated under FB (see Fig. 3b) by modulating I_p (see Fig. 3e). Similarly, the q_0 evolution tracks its target $\bar{q}_0$ during the FF + FB simulation (see Fig. 3c), while such tracking is not found in the FF-only simulation. To regulate q_0, j_{q_0} is varied under FB (see Fig. 3f), although convergence toward the j_{q_0} target is not achieved until around $t \geq 4$ s. Still, good q_0 control is achieved possibly due to the nonlinear controller synthesis, which may allow for driving the system to the same final state despite using different input trajectories. Because COTSIM simulates a time-varying equilibrium and uses different transport models (see Section 5.1) than the ones employed by the FB controllers (see Section 3), robustness against unknown dynamics is demonstrated in these simulation results. Moreover, it must be noted that all P_{tot}, I_p, and j_{q_0} are driven close to the target inputs during the FF + FB simulation, although the FB controllers do not receive any information about such target inputs.

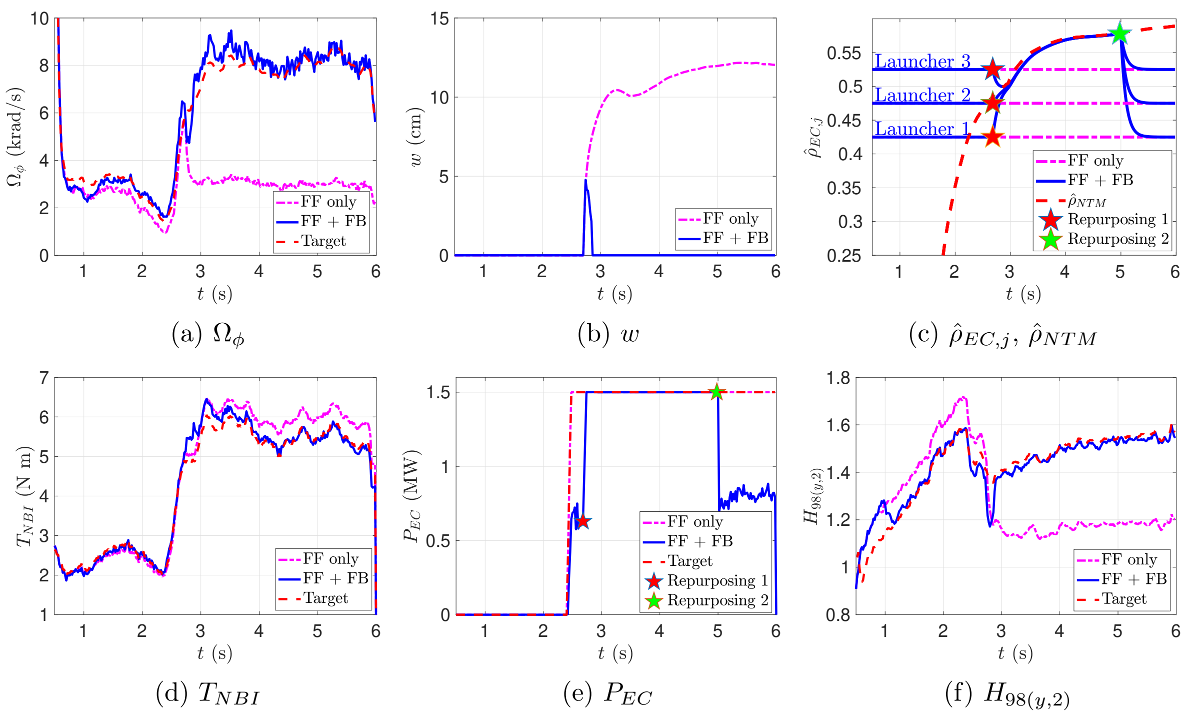

(a) Ω_ϕ (b) w (c) $\hat{\rho}_{EC,j}$, $\hat{\rho}_{NTM}$

(d) T_{NBI} (e) P_{EC} (f) $H_{98(y,2)}$

Figure 4: Time evolutions for Ω_ϕ, w, $\hat{\rho}_{EC,j}$, $\hat{\rho}_{NTM}$, T_{NBI}, P_{EC}, and $H_{98(y,2)}$ in FF-only (magenta dashed-dotted) and FF + FB (blue solid) during simulations using COTSIM, together with the target evolutions (red dashed).

Fig. 4 show the evolution of Ω_ϕ and w together with their respective high-level actuation requests from the individual-scalar controllers, T_{NBI} and P_{EC}. In addition,

Fig. 4 shows $\hat{\rho}_{EC,j}$, $\hat{\rho}_{NTM}$, and $H_{98(y,2)}$ (calculated from the IPB98(y,2) scaling law as $H_{98(y,2)} = \frac{W}{KP_{tot}}$, where K is given by $K = 0.0562 I_p^{0.93} B_{\phi,0}^{0.15} R_0^{1.97} \epsilon^{0.58} \bar{n}_e^{0.41} \kappa^{0.78} A_{eff}^{0.19} P_{tot}^{-0.69}$). Under FB, Ω_ϕ is driven toward its target $\bar{\Omega}_\phi$ (see Fig. 4a) despite temporary deviations due to the effects of the NTM. In the FF-only case, Ω_ϕ suffers a substantial decrease as a result of the NTM. On the other hand, w is driven to zero under FB (see Fig. 4b) by increasing P_{EC} (see Fig. 4e) and steering the ECH&CD deposition toward the spatial location of the mode (see Fig. 4c) at $t = 2.7$ s, when the three ECH&CD launchers are repurposed from individual-scalar control to NTM active suppression. It can be observed that $w = 0$ is reached at $t \approx 2.85$ s and, after that, $\hat{\rho}_{EC,j}$ keep pre-emptive tracking of $\hat{\rho}_{NTM}$ until $t = 5s$ ($N_{EC,pre} = 3$). At $t = 5$ s, $\hat{\rho}_{EC,j}$ return back to their individual-scalar-control values. Without activation of the NTM-suppression controller in the FF-only simulation, the island grows and saturates with $w \geq 10$ cm. Also, $H_{98(y,2)}$ is higher during the flat-top of the FF + FB simulation (see Fig. 4f) as a result of the combined individual-scalar + NTM-suppression control.

Fig. 5 shows the evolution of P_{NBI}^{ON}, P_{NBI}^{150}, and P_{NBI}^{210}. As introduced earlier, these NBI powers are modulated for the regulation of W, q_0, and Ω_ϕ. It can be observed that the values during the FF + FB simulation are driven very close to the target evolutions. However, the FF + FB and target evolutions are not the same and sometimes drift away slightly, mainly due to the NTM development when $t \in [2.7, 4]$ s (particularly for the 150, co-current off-axis beamline, see Fig. 5b). Moreover, such drifts are also caused by the temporary use of the 210 beamline (see Fig. 5c), whose counter-current drive is necessary to allow for Ω_ϕ regulation. Still, it can be seen that P_{NBI}^{ON} remains close to its target (see Fig. 5a) and P_{NBI}^{210} tends to zero as the simulation advances, despite moderate fluctuations. These fluctuations are caused by the measurement noise, but are minimized by the use of low-pass filters within the FB controllers. In addition, it can be observed that smooth actuator trajectories are ensured by the actuator manager, e.g. as P_{NBI}^{150} is increased at $t = 5$ s (see Fig. 5b) when P_{EC} is abruptly reduced (see Fig. 4e) in order to maintain a smooth P_{tot} trajectory for W control (see Fig. 4a and 4d).

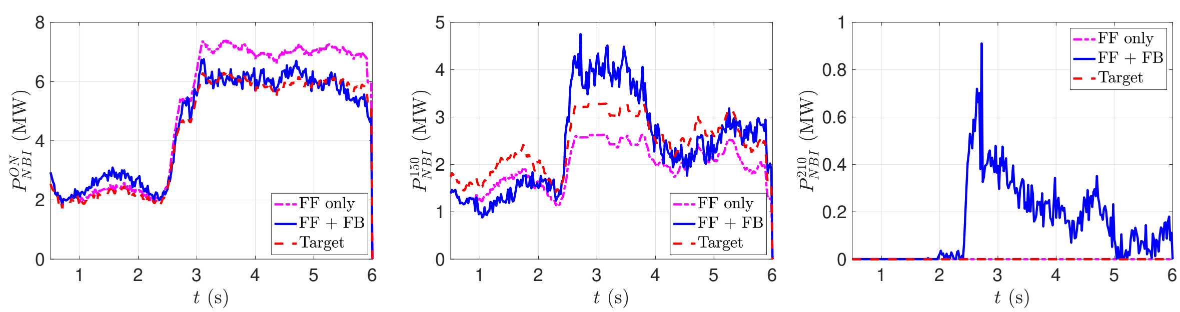

(a) P_{NBI}^{ON} (b) P_{NBI}^{150} (c) P_{NBI}^{210}

Figure 5: Time evolutions for P_{NBI}^{ON}, P_{NBI}^{150}, and P_{NBI}^{210} in FF-only (magenta dashed-dotted) and FF + FB (blue solid) during simulations using COTSIM, together with the target evolutions (red dashed).

6. Experimental Testing of the Integrated Architecture in DIII-D

The control architecture has been experimentally tested in the high-q_{min} scenario in DIII-D. The same NBI groups as in simulation were employed (whose powers are denoted by P_{NBI}^{ON}, P_{NBI}^{150}, and P_{NBI}^{210}). However, it must be taken into account that some of the NBIs and ECH&CD launchers that were used for FB control in simulations could not be employed for FB control in experiments. First, in order to have an accurate real-time q-profile reconstruction, a particular modulation of the 30 beamline was required that interferred with its use for FB control. Second, one of the NBIs in the 330 beamline must be regulated in a particular fashion to provide ω_ϕ measurements. Thus, only about 2 MW within P_{NBI}^{ON} could be employed for FB control, which yielded less controllability than in simulations for the individual scalars. Finally, two ECH&CD launchers were available during these experiments ($N_{EC} = 2$). This limited the maximum available P_{EC} to about 1 MW. Like in simulations, both ECH&CD launchers were used entirely for active-suppression mode ($N_{EC,pre} = 0$), or entirely in pre-emptive suppression mode ($N_{EC,pre} = 2$), and are set up to do individual-scalar control at the beginning of the shot.

Two shots are compared in this section: a FF-only shot (185362) and a FF + FB shot (185374). Similarly to the simulation study in Section 5.2, an H-mode plasma with relatively lower performance was found during the FF-only shot. Targets are chosen for the individual scalars that are significantly far from the evolutions obtained under FF-only, and the FB scheme is employed to test if, by means of FF + FB, a higher performance plasma can be obtained. Whereas the FB controllers for W, q_0, and q_e are turned on at $t = 0.9$ s, regulation of Ω_ϕ is turned on when $t \geq 4$ s. This change in the active control tasks is meant to test the capabilities of the scheme to do simultaneous multiple-mission sharing of the NBIs (see Section 4.4). In addition, a failure in one of the NBIs within the 150 beamline is emulated from $t = 3$ s until $t = 3.75$ s during the FF + FB shot. Such actuator failure, which is totally unexpected by the FF + FB control scheme, is included to test the capabilities of the architecture to do repurposing sharing while still achieving the desired target plasma. Moreover, the ONFR system monitors the plasma state during the FF + FB shot in order to detect possible $n = 2$ MHD activity and, if needed, command the AM algorithm to do repurposing sharing of the ECH&CD for NTM suppression. In such case, the ECH&CD poloidal mirrors are steered toward the $q = 3/2$ surface, which is considered as a surface prone to tearing in this case. Just like in the simulation study, it must be kept in mind that the FB controllers use FF inputs that are very similar to those employed during the FF-only shot, but the FB controllers do not have any knowledge about the inputs associated with the target.

Fig. 6 shows the evolution of W, q_e, and q_0 together with their respective high-level actuation requests from the individual-scalar controllers, P_{tot}, I_p, and j_{q_0}. Differences in the plasma formation and early stage of the discharge make W and q_e have slightly different values in FF-only and FF + FB when the FB is turned on $t = 0.9$ s. During

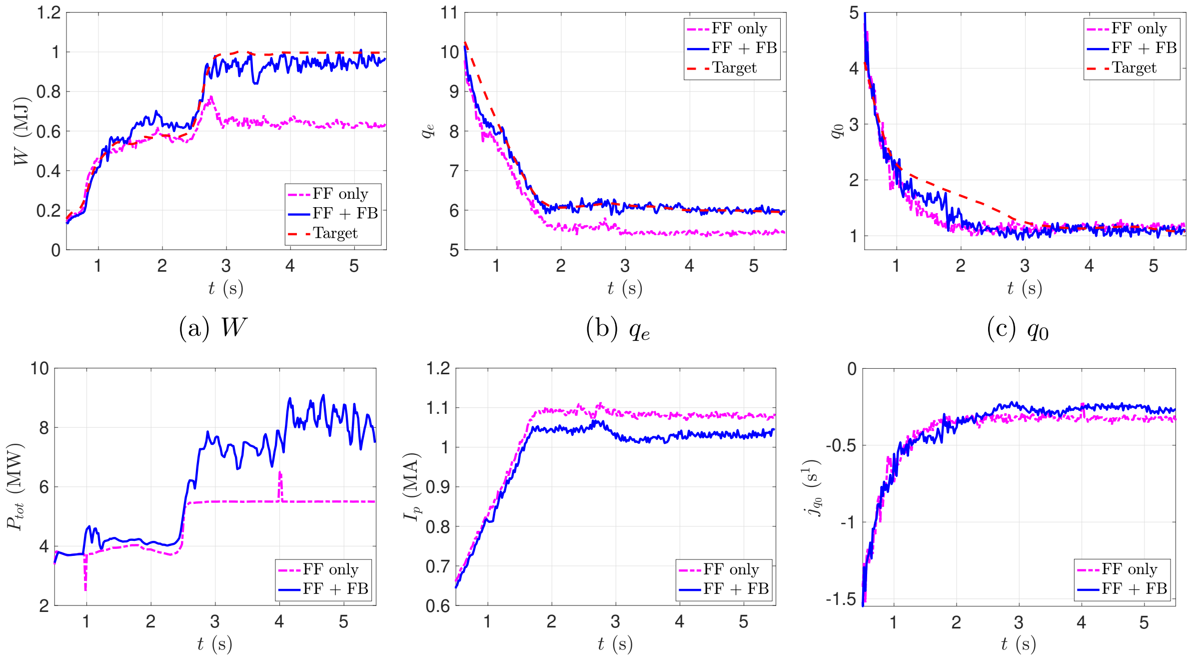

(a) W (b) q_e (c) q_0

(d) P_{tot} (e) I_p (f) j_{q_0}

Figure 6: Time evolutions for W, q_e, q_0, P_{tot}, I_p, and j_{q_0} in FF-only (magenta dashed-dotted) and FF + FB (blue solid) during DIII-D experiments, together with the targets (red dashed). The FF-only shot is 185362 and the FF + FB shot is 185374.

the FF-only shot, the plasma confinement is worsened due to MHD modes with $n = 1$ (not shown in this paper) and $n = 2$ (shown in Fig. 7). Although NTMs often appear in these high-q_{min} plasmas [25] and the control scheme in this work was specially designed for their suppression, the modes in shots 185362 and 185374 are most likely TMs rather NTMs. The reason for this is that TMs often appear earlier in the discharge, when W and the bootstrap current are relatively low, whereas NTMs usually develop with higher W, e.g. around $t \approx 2.5$ s when W is rapidly increased. Because the control synthesis carried out in Section 4.1.2 assumes an NTM dynamics, the NTM-suppression controller will be, in general, less effective against TMs and will not necessarily guarantee the desired rate of suppression, $\tau \triangleq 1/(a_2 K_P^w)$. In any case, during the FF + FB shot, the W controller increases P_{tot} in order to increase W, achieving good W control for a relatively short period of time (until about $t = 1.5$ s, see Fig. 6a and 6d). After that (1.5 s $\leq t \leq 2.5$ s), W increases beyond its target $\bar{W}$ and the FB scheme apparently does not try to correct this by reducing P_{tot}. Such behavior is due to the simultaneous-multiple mission sharing of the NBIs and ECH&CD for W and q_0 control (see Fig. 6c). Because q_0 and W have the same control priority, both control tasks are carried out in the best possible way. On the one hand, if P_{tot} was reduced much further, then q_0 would also be reduced, yielding poor q_0-control performance. On the other hand, if P_{tot} was increased, then better q_0 tracking would be achieved, but W would be increased too much and poor W-control performance would be found. The intermediate solution, which is the one adopted by the control architecture in the FF + FB shot, is having slightly higher W and slightly lower q_0 than their targets. Later on, when $t \geq 2.5$ s, the performance of the W controller becomes significantly better due to the compatibility of the q_0 and W control tasks, which both require an increase in P_{tot}. The evolution of W is kept close to its target in the FF + FB shot despite the MHD phenomena present in this plasma. However, the steady-state error for W does not converge to zero, although it is small (about $\tilde{W} \approx -0.05$ MJ). This error could be further reduced by increasing the integral gain K_I^1 and decreasing ϵ_1 (see Section 4.1.1), but the associated oscillations in P_{tot} would become unacceptable and promote even higher MHD activity. During this experiment, the small W steady-state error under FF + FB was unavoidable, and in any case, the W error was significantly reduced with respect to the FF-only case. Regarding q_0, it initially gets closer to its target during the FF + FB shot (when $t < 2$ s, see Fig. 6c) than in the FF-only shot, but very low response to actuation was found after $t \geq 2$ s. In these shots, q_0 converged to approximately the same final value, regardless of the j_{q0} evolution (see Fig. 6f). This lack of q_0 controllability is partially due to the smaller FB power available during the experiment when compared to simulations. In contrast, q_e is successfully regulated under FB (see Fig. 6b) by means of I_p, which is reduced in the FF + FB shot with respect to the FF-only case (see Fig. 6e). Accurate q_e control is achieved despite variations in the plasma equilibrium and significant MHD activity, demonstrating the robustness of the control scheme. Lower I_p values contribute to slightly higher P_{tot} values during the FF + FB shot, as the plasma temperature slightly decreases and requires additional NBI power to sustain W. Moreover, the additional P_{tot} and higher W, specially after $t \geq 2.5$ s, also contribute to the low responsiveness of q_0 to the FB actuation, as η becomes relatively low, making $\partial\psi/\partial t \to 0$ and freezing the q profile (see the magnetic-diffusion equation (A.1) in Appendix A). Therefore, the combination of low FB-power availability and low η made the q_0 controllability quite low in this experiment.

Fig. 7 shows the evolution of Ω_ϕ and $n = 2$ MHD amplitude together with their respective high-level actuation requests from the individual-scalar controllers, T_{NBI} and P_{EC}. In addition, Fig. 7 shows $\hat{\rho}_{EC,j}$, $\hat{\rho}_{NTM}$, and $H_{98(y,2)}$. During the FF-only shot, Ω_ϕ is much lower (see Fig. 7a) due to the effects of the MHD activity (see Fig. 7b). During the FF + FB shot, T_{NBI} is modified (see Fig. 7d) to try to regulate Ω_ϕ. It can be observed that there is an initial overshoot in T_{NBI} that the controller corrects afterwards, until reaching a stationary T_{NBI} value and approximately constant steady-state error for Ω_ϕ (around $\tilde{\Omega}_\phi \approx -0.5$ krad/s). This indicates a low integral gain K_I^4 and/or a too high ϵ_4 (see Section 4.1.1), which do not allow for driving $\tilde{\Omega}_\phi$ closer to 0. The proportional and integral gains used during the experiment were tuned previously in simulations, but a slightly different control performance was achieved most likely due to the differences in MHD activity. In any case, the FF + FB shot has values of Ω_ϕ closer to the target than the FF-only shot. It can also be seen that the simultaneous multiple-mission sharing of the NBI and EC powers for W, q_0, and Ω_ϕ regulation is successfully carried out without loss of control performance. In addition, ONFR correctly detects the potentially problematic MHD activity in the FF + FB shot at $t \approx 2.65$ s, and the ECH&CD is repurposed to do active suppression by increasing P_{EC} (see Fig. 7e) and

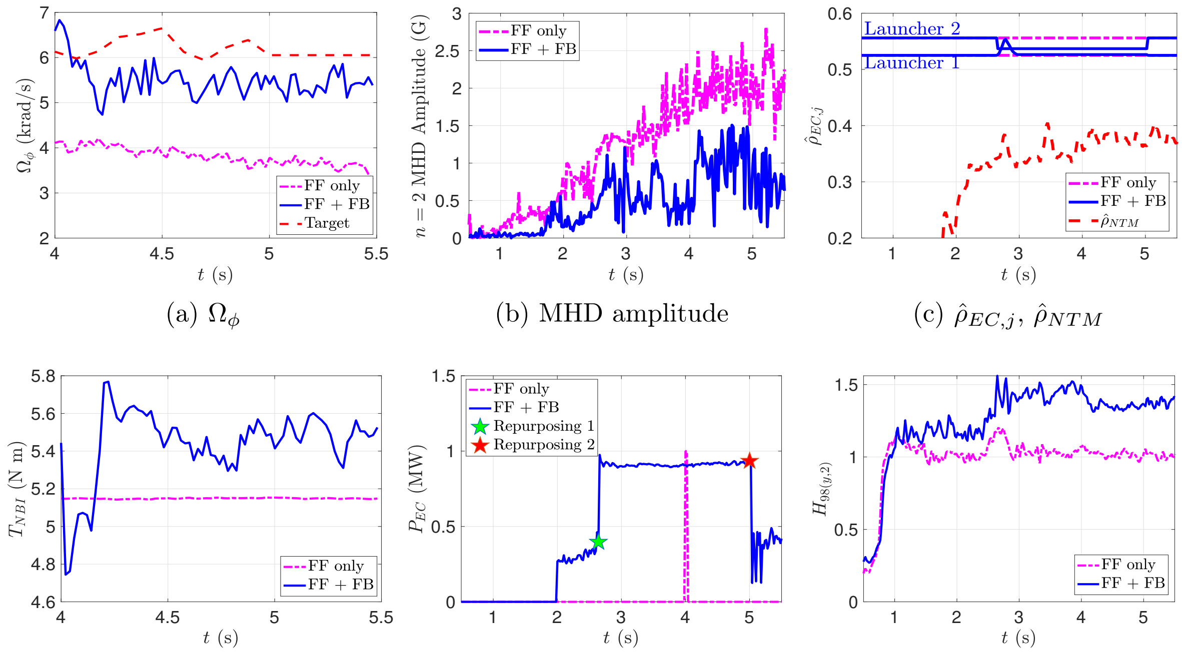

(a) Ω_ϕ (b) MHD amplitude (c) $\hat{\rho}_{EC,j}$, $\hat{\rho}_{NTM}$

(d) T_{NBI} (e) P_{EC} (f) $H_{98(y,2)}$

Figure 7: Time evolutions for Ω_ϕ, $n = 2$ MHD amplitude, $\hat{\rho}_{EC,j}$, $\hat{\rho}_{NTM}$, T_{NBI}, P_{EC}, and $H_{98(y,2)}$ in FF-only (magenta dashed-dotted) and FF + FB (blue solid) during DIII-D experiments. The FF-only shot is 185362 and the FF + FB shot is 185374.

steering the ECH&CD launchers (see Fig. 7c). However, it can be appreciated that the ECH&CD launchers are not correctly steered by the NTM-suppression controller toward the $q = 3/2$ surface due to a PCS setup issue. Despite this, the control-priority switch (repurposing sharing) within the integrated architecture did function properly during the experiment, which is a verification of the scheme's capability to handle real-time changes in the control priorities. Also, it can be seen that the $n = 2$ MHD amplitude (see Fig. 7b) is reduced in the FF + FB shot and kept lower than in the FF-only case. Although this partial reduction in MHD activity is most likely a result of the increased P_{EC} rather than of the localized ECH&CD (see [30], where tearing stability was improved in these plasmas using mid-radius ECCD), it is not clear what the MHD activity would have been like if the NTM-suppression controller had steered the ECH&CD correctly, as the FF-only and FF + FB plasmas look really different right from the beginning of the discharge in terms of MHD activity. Moreover, P_{EC} was quite low during this experiment and may not have sufficed for TM/NTM suppression in this DIII-D scenario [30]. Pre-emptive suppression was never activated in the experiment due to the lack of effectiveness in suppressing the mode. The ONFR system was set up in an off-line fashion to determine that, at $t = 5$ s, the ECH&CD launchers were repurposed again. As a result of lower MHD activity and different individual-scalar evolutions, which were maintained under FB regulation, $H_{98(y,2)}$ is significantly higher in the FF + FB shot compared to the FF-only shot (see Fig. 7f). When the 210 beamline is employed at $t \geq 4$ s in the FF + FB shot, a slight increase in MHD amplitude and a decrease in $H_{98(y,2)}$ can be observed, although these never reach the FF-only levels.

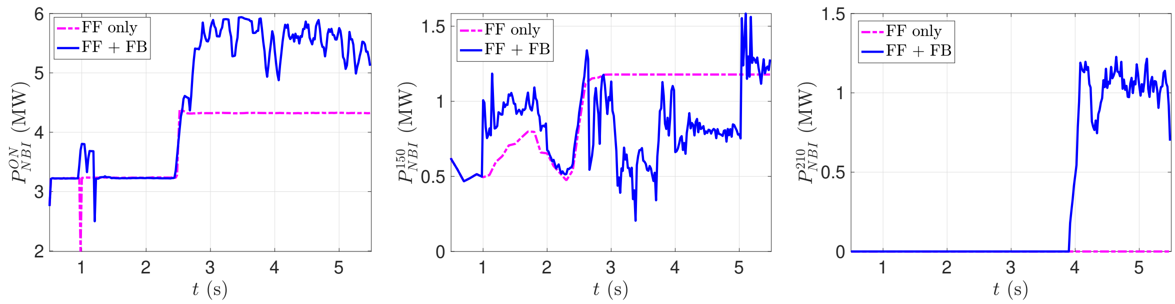

(a) P_{NBI}^{ON} (b) P_{NBI}^{150} (c) P_{NBI}^{210}

Figure 8: Time evolutions for P_{NBI}^{ON}, P_{NBI}^{150}, and P_{NBI}^{210} in FF-only (magenta dashed-dotted) and FF + FB (blue solid) during DIII-D experiments. The FF-only shot is 185362 and the FF+FB shot is 185374.

Fig. 8 shows the evolution of P_{NBI}^{ON}, P_{NBI}^{150}, and P_{NBI}^{210}. Initially, there is little modulation of P_{NBI}^{ON} (see Fig. 8a), but P_{NBI}^{150} is substantially increased (see Fig. 8b) for q_0 regulation. This is in accordance with the W and q_0 control compromise. At around $t = 2.65$ s, when ECH&CD is repurposed for NTM suppression, P_{NBI}^{ON} is substantially increased to keep W around its target. Also, at $t = 3$ s, the emulated partial failure of the 150 beamline happens, which accounts for a loss of about 0.5 MW within P_{NBI}^{150}. This is substituted by P_{NBI}^{ON} until $t = 3.75$ s, when P_{NBI}^{150} increases again and P_{NBI}^{ON} decreases. At $t = 4$ s, when P_{NBI}^{210} comes on (see Fig. 8c), the other NBI powers are adapted by the AM algorithm in order to maintain the plasma-control performance. At $t = 5$ s, P_{NBI}^{150} is suddenly increased (see Fig. 8b) to compensate for the decrease in P_{EC} (see Fig. 7e), maintaining P_{tot} at similar levels. The actuator manager is capable of recognizing that both actuators provide a source of off-axis current and heating. This helps maintaining the desired W and q_0 evolutions (see Fig. 6a and 6c) with the appropriate P_{tot} and j_{q_0} trajectories (see Fig. 6d and 6f).

7. Conclusions and Possible Future Work

An integrated-control architecture has been developed that has functionalities which will be necessary for future PCSs found in burning-plasma tokamaks. It allows for simultaneously executing nonlinear-robust controllers for kinetic, magnetic, and MHD-related aspects of the plasma dynamics, together with actuator management as well as supervisory and exception handling functions. Therefore, the architecture can perform both continuous and off-normal control functions. The architecture has been implemented within the DIII-D PCS, which is a world-leading benchmark for control development. Experiments in the DIII-D high-q_{min} scenario, which possesses some of the necessary characteristics for steady-state operation in ITER and beyond, have been carried out with satisfactory control performance. These experimental results suggest that the use of integrated-control strategies may help to reproduce and achieve the high-performance plasmas required in economically viable fusion power plants. The use of model-based, nonlinear-robust control techniques may have enabled such control performance by retaining the nonlinear information of the control-synthesis plasma models, while also taking into account the limitations in the understanding of the plasma-physics phenomena. Simulations using COTSIM have been executed to enable pre-experimental tuning of the feedback controllers and assess the overall architecture's performance beforehand, saving valuable experimental time. By means of extensive modeling using nonlinear simulation models (that simulate most of the plasma-dynamics aspects, like 1D current, heat, and particle transport, 0D pedestal evolution and magnetic-island growth, and 2D plasma equilibrium), a more realistic and effective simulation testing has been attained that qualitatively reproduces the plasma behavior observed in real experiments.

Future work may include the expansion of the available controllers and actuators within the integrated architecture (e.g. shape control, 3D coils, gas puffing/pellet injection, pedestal/edge-localized mode control, etc.) as well as an extended PCS architecture allowing for broader S&EH (e.g. monitoring and detection of edge-localized modes) and AM capabilities. In addition, the inclusion of other important physics phenomena within the control-synthesis model will be studied. For example, although high rotation values have been explored in this work, the addition of the rotation-dynamics effects on NTM-island width stability could highly benefit the performance of the integrated-control architecture in low-rotation scenarios found in future reactors.

Acknowledgments

This material is based upon work supported by the U.S. Department of Energy, Office of Science, Office of Fusion Energy (DE-SC0010661, DE-FC02-04ER54698). The authors would like to acknowledge useful advice and help from William P. Wehner, Allan W. Hyatt, Robert J. La Haye, Heather Shen, and Benjamin Penaflor (General Atomics) regarding implementation in the DIII-D PCS and testing of the algorithms in this work.

thereof.

Appendix A. Magnetic Diffusion Modeling

The basic equation that models the dynamics of the magnetic plasma variables in this work is the magnetic diffusion equation [24], which together with its boundary conditions, can be written as

$$\frac{\partial \psi}{\partial t} = \frac{\eta}{\mu_0 \rho_b^2 \hat{F}^2} \frac{1}{\hat{\rho}} \frac{\partial}{\partial \hat{\rho}} \left(\hat{\rho} \hat{F} \hat{G} \hat{H} \frac{\partial \psi}{\partial \hat{\rho}} \right) + R_0 \hat{H} \eta \left(\sum_{i=1}^{i=N_{NBI}} j_{NBI,i} + \sum_{j=1}^{j=N_{EC}} j_{EC,j} + j_{BS} \right), \quad \text{(A.1)}$$

$$\left. \frac{\partial \psi}{\partial \hat{\rho}} \right|_{\hat{\rho}=0} = 0, \qquad \left. \frac{\partial \psi}{\partial \hat{\rho}} \right|_{\hat{\rho}=1} = -\frac{\mu_0 R_0}{\hat{G}(\hat{\rho}=1)\hat{H}(\hat{\rho}=1)} I_p \triangleq -k_{I_p} I_p, \quad \text{(A.2)}$$

where $\psi \triangleq \Psi/(2\pi)$ is the poloidal stream function, t is the time, η is the plasma resistivity, μ_0 is the vacuum permeability, R_0 is the major radius, $j_{NBI,i}$ is the current density deposited by the i-th NBI group ($i = 1, ..., N_{NBI}$, where N_{NBI} is the total number of NBI groups), $j_{EC,j}$ is the current density deposited by the j-th EC launcher ($j = 1, ..., N_{EC}$, where N_{EC} is the total number of EC launchers), j_{BS} is the bootstrap current-density, $\hat{F}$, $\hat{G}$, and $\hat{H}$ are geometric factors of the plasma equilibrium, and $k_{I_p} \triangleq \frac{\mu_0 R_0}{\hat{G}(\hat{\rho}=1)\hat{H}(\hat{\rho}=1)}$ is a model parameter. In this control-synthesis model, it is assumed that the geometric factors $\hat{F}$, $\hat{G}$, and $\hat{H}$ do not vary significantly in time, i.e. a fixed equilibrium is considered. However, the inclusion of model uncertainties, as introduced later in this section, enables a robust-control design for plasmas with time-varying equilibriums. Moreover, during the simulation testing using COTSIM (see Section 5), a two-dimensional, time-varying equilibrium is in fact employed.

Physics-based, control-oriented models [31] are used for η, $j_{NBI,i}$, $j_{EC,j}$, and j_{BS}, as given by

$$\eta = \frac{k_{sp} Z_{eff}}{T_e^{3/2}}, \quad j_{NBI,i} = j_{NBI,i}^{dep} \frac{\sqrt{T_e}}{n_e} P_{NBI,i}, \quad j_{EC,j} = j_{EC,j}^{dep}\left(\hat{\rho}_{EC,j}\right) \frac{T_e}{n_e} P_{EC,j}, \quad \text{(A.3)}$$

$$j_{BS} = \frac{R_0}{\hat{F}} \left(\frac{\partial \psi}{\partial \hat{\rho}} \right)^{-1} \left[2\mathcal{L}_{31} T_e \frac{\partial n_e}{\partial \hat{\rho}} + \left(2\mathcal{L}_{31} + \mathcal{L}_{32} + \alpha \mathcal{L}_{34}\right) n_e \frac{\partial T_e}{\partial \hat{\rho}} \right], \quad \text{(A.4)}$$

where k_{sp} and $j_{NBI,i}^{dep}$ are constant model profiles, Z_{eff} is the effective atomic number of the plasma ions, $j_{EC,j}^{dep}$ are model profiles that depend on $\hat{\rho}_{EC,j}$, T_e and n_e are the electron temperature and density, respectively, and $\mathcal{L}_{31}$, $\mathcal{L}_{32}$, $\mathcal{L}_{34}$, and α are geometric factors of the plasma equilibrium [37].

In some tokamaks, steerable mirrors allow for changing the EC aiming so that the ECH&CD region varies. In particular, poloidal mirrors allow for sweeping the ECH&CD region along the poloidal cross-section. In this work, $\hat{\rho}_{EC,j}$ ($j = 1, ..., N_{EC}$) are considered as inputs that can be controlled in real time and determine the aiming location of the ECCD system. In the control-oriented model for ECH&CD given by (A.3), the function $j_{EC,j}^{dep}(\hat{\rho}_{EC,j})$ reflects the changes associated with poloidal-mirror steering, and the maximum value of $j_{EC,j}$ across the $\hat{\rho}$ domain is denoted as $j_{EC,j}^{max}$. In addition, $j_{EC,j}^{dep}(\hat{\rho}_{EC,j})$ and its changes with poloidal-mirror steering can be qualitatively described as shown in Fig. A1, where the j subindex has been dropped for simplicity. The location of the maximum of $j_{EC}^{dep}(\hat{\rho}_{EC})$ is denoted by $\hat{\rho}^{max}$, whereas the location of the mean of the ECH&CD distribution is equal to $\hat{\rho}_{EC}$. Both $\hat{\rho}^{max}$ and $\hat{\rho}_{EC}$ are usually very close but, in general, they are different because $j_{EC}^{dep}(\hat{\rho}_{EC})$ is not perfectly symmetric about its mean. In addition, when $\hat{\rho}_{EC}$ is steered from a first value $\hat{\rho}_{EC}^{0}$ to a second value $\hat{\rho}_{EC}^{1}$, the j_{EC}^{dep} profile is shifted in space (and so is $\hat{\rho}^{max}$, which goes from $\hat{\rho}^{max,0}$ to $\hat{\rho}^{max,1}$), but its shape and its maximum value do not change (i.e. $j_{EC}^{dep}(\hat{\rho}^{max,0}) = j_{EC}^{dep}(\hat{\rho}^{max,1})$). It must be taken into account that, in general, the location of $j_{EC,j}^{max}$ may not be the same as $\hat{\rho}^{max}$.

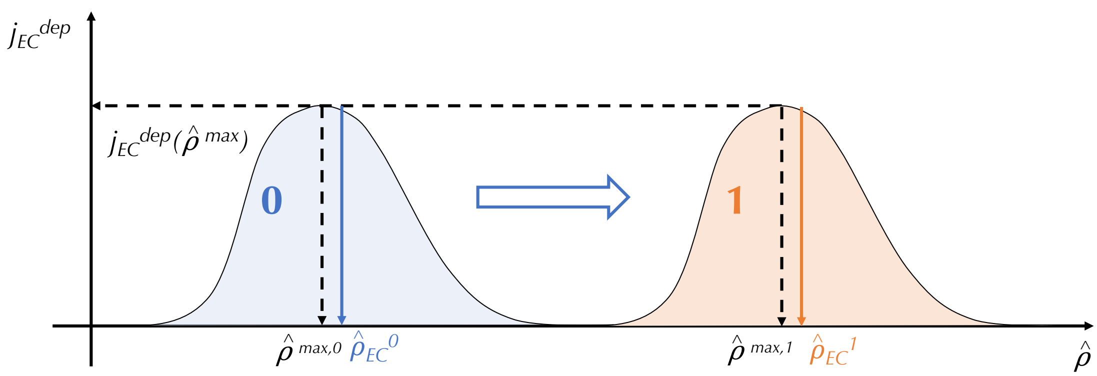

Figure A1: Diagram showing $j_{EC}^{dep}(\hat{\rho}_{EC})$, $\hat{\rho}_{EC}$, and $\hat{\rho}^{max}$ when poloidal-mirror steering is carried out from position 0 to position 1.

To close the model, the evolutions of n_e and T_e are modeled as

$$n_e(\hat{\rho},t) = n_e^{prof}(\hat{\rho})\bar{n}_e(t) + \delta_{n_e}(\hat{\rho},t), \tag{A.5}$$

$$T_e(\hat{\rho},t) = T_e^{prof}(\hat{\rho})I_p(t)\sqrt{P_{tot}(t)}\;\bar{n}_e^{-1}(t) + \delta_{T_e}(\hat{\rho},t), \tag{A.6}$$

where n_e^{prof} and T_e^{prof} are model profiles, $\bar{n}_e$ is the line-average electron density (for which an estimation is assumed to be available in real time, so it is treated as a non-controlled input to the model), $P_{tot} = \sum_i P_{NBI,i} + \sum_j P_{EC,j}$ is the total injected power, and δ_{n_e} and δ_{T_e} are uncertainties that bundle inaccuracies in the modeling process (e.g. unmodeled electron particle and heat sources, unexpected changes in electron confinement, MHD instabilities, etc.). More concretely, δ_{n_e} and δ_{T_e} can be interpreted like terms that model the difference between the actual density and temperature values during a shot (i.e. n_e and T_e) and the estimations given by the control-oriented scalings $n_e^{nom} \triangleq n_e^{prof}\bar{n}_e$ and $T_e^{nom} \triangleq T_e^{prof}I_p\sqrt{P_{tot}}\,\bar{n}_e^{-1}$, respectively.

The uncertainties δ_{n_e} and δ_{T_e} introduced in (A.5)-(A.6) yield uncertainties in η, $j_{NBI,i}$, $j_{EC,j}$, and j_{BS}, so the overall magnetic-diffusion dynamics is uncertain with

$$\eta = \frac{k_{sp}^{prof}Z_{eff}}{(T_e^{nom}+\delta_{T_e})^{3/2}} \triangleq \frac{k_{sp}^{prof}Z_{eff}}{(T_e^{nom})^{3/2}} + \delta_{\eta}, \tag{A.7}$$

$$j_{NBI,i} = j_{NBI,i}^{dep}\frac{\sqrt{T_e^{nom}+\delta_{T_e}}}{n_e^{nom}+\delta_{n_e}}P_{NBI,i} \triangleq j_{NBI,i}^{dep}\frac{\sqrt{T_e^{nom}}}{n_e^{nom}}P_{NBI,i} + \delta_{j_{NBI,i}}, \tag{A.8}$$

$$j_{EC,j} = j_{EC,j}^{dep} \frac{T_e^{nom} + \delta_{T_e}}{n_e^{nom} + \delta_{n_e}} P_{EC,j} \triangleq j_{EC,j}^{dep} \frac{T_e^{nom}}{n_e^{nom}} P_{EC,j} + \delta_{j_{EC,j}}, \tag{A.9}$$

$$\begin{aligned} j_{BS} &= \frac{R_0}{\hat{F}} \left(\frac{\partial \psi}{\partial \hat{\rho}} \right)^{-1} \Big[2\mathcal{L}_{31} \frac{\partial (T_e^{nom} + \delta_{T_e})}{\partial \hat{\rho}} (n_e^{nom} + \delta_{n_e}) \\ &+ (2\mathcal{L}_{31} + \mathcal{L}_{32} + \alpha \mathcal{L}_{34}) \frac{\partial (n_e^{nom} + \delta_{n_e})}{\partial \hat{\rho}} (T_e^{nom} + \delta_{T_e}) \Big] \\ &\triangleq \frac{R_0}{\hat{F}} \left(\frac{\partial \psi}{\partial \hat{\rho}} \right)^{-1} \left[2\mathcal{L}_{31} \frac{\partial T_e^{nom}}{\partial \hat{\rho}} n_e^{nom} + (2\mathcal{L}_{31} + \mathcal{L}_{32} + \alpha \mathcal{L}_{34}) \frac{\partial n_e^{nom}}{\partial \hat{\rho}} T_e^{nom} \right] + \delta_{j_{BS}}, \end{aligned} \tag{A.10}$$

where

$$\delta_\eta \triangleq \frac{k_{sp}^{prof} Z_{eff} [(T_e^{nom})^{3/2} - (T_e^{nom} + \delta_{T_e})^{3/2}]}{[T_e^{nom}(T_e^{nom} + \delta_{T_e})]^{3/2}}, \tag{A.11}$$

$$\delta_{j_{NBI,i}} \triangleq j_{NBI,i}^{dep} P_{NBI,i} \left(\frac{\sqrt{T_e^{nom} + \delta_{T_e}}}{n_e^{nom} + \delta_{n_e}} - \frac{\sqrt{T_e^{nom}}}{n_e^{nom}} \right), \tag{A.12}$$

$$\delta_{j_{EC,j}} \triangleq j_{EC,j}^{dep} P_{EC,j} \left(\frac{T_e^{nom} + \delta_{T_e}}{n_e^{nom} + \delta_{n_e}} - \frac{T_e^{nom}}{n_e^{nom}} \right), \tag{A.13}$$

$$\begin{aligned} \delta_{j_{BS}} \triangleq \frac{R_0}{\hat{F}} \left(\frac{\partial \psi}{\partial \hat{\rho}} \right)^{-1} \Bigg[& 2\mathcal{L}_{31} \left(\frac{\partial \delta_{T_e}}{\partial \hat{\rho}} (n_e^{nom} + \delta_{n_e}) + \frac{\partial T_e^{nom}}{\partial \hat{\rho}} \delta_{n_e} \right) + \\ & (2\mathcal{L}_{31} + \mathcal{L}_{32} + \alpha \mathcal{L}_{34}) \left(\frac{\partial \delta_{n_e}}{\partial \hat{\rho}} (T_e^{nom} + \delta_{T_e}) + \frac{\partial n_e^{nom}}{\partial \hat{\rho}} \delta_{T_e} \right) \Bigg]. \end{aligned} \tag{A.14}$$

For convenience, a total non-inductive uncertainty is defined as the sum of the uncertainties related with the NBI, EC, and bootstrap current densities, i.e.

$$\delta_{j_{ni}} \triangleq \sum_{i=1}^{i=N_{NBI}} \delta_{j_{NBI,i}} + \sum_{j=1}^{j=N_{EC}} \delta_{j_{EC,j}} + \delta_{j_{BS}}. \tag{A.15}$$

A model for q_0 can be obtained as follows. First, plugging equations (A.3)-(A.4) and (A.5)-(A.6) into the magnetic-diffusion equation (A.1) yields

$$\begin{aligned} \frac{\partial \psi}{\partial t} &= f_{\eta,1}(\hat{\rho}) \frac{\partial}{\partial \hat{\rho}} \left(f_{\eta,2}(\hat{\rho}) \frac{\partial \psi}{\partial \hat{\rho}} \right) u_\eta(t) + \sum_{i=1}^{i=N_{NBI}} f_{NBI,i}(\hat{\rho}) u_{NBI,i}(t) \\ &+ \sum_{j=1}^{j=N_{EC}} f_{EC,j}(\hat{\rho}, \hat{\rho}_{EC,j}) u_{EC,j}(t) + \left(\frac{\partial \psi}{\partial \hat{\rho}} \right)^{-1} f_{BS}(\hat{\rho}) u_{BS}(t) + \delta_\psi, \end{aligned} \tag{A.16}$$

where the terms u_η, $u_{NBI,i}$, $u_{EC,j}$, and u_{BS} are virtual inputs that depend on the physical inputs (i.e I_p, $P_{NBI,i}$, $P_{EC,j}$, and $\bar{n}_e$) as given by (4)-(5), the definitions of $f_{\eta,1}$, $f_{\eta,2}$, $f_{NBI,i}$, $f_{EC,j}$, and f_{BS} in terms of the other model functions and parameters are given by

$$f_{\eta,1} \triangleq \frac{k_{sp}}{\mu_0 \rho_b^2 \hat{F}^2} \frac{Z_{eff}}{(T_e^{prof})^{\frac{3}{2}}} \frac{1}{\hat{\rho}}, \quad f_{\eta,2} \triangleq \hat{\rho} \hat{F} \hat{G} \hat{H}, \tag{A.17}$$

$$f_{NBI,i} \triangleq R_0 \hat{H} k_{sp} \frac{Z_{eff}}{T_e^{prof} n_e^{prof}} j_{NBI,i}^{dep}, \quad f_{EC,j} \triangleq R_0 \hat{H} k_{sp} \frac{Z_{eff}}{\sqrt{T_e^{prof}} n_e^{prof}} j_{EC,j}^{dep}, \tag{A.18}$$

$$f_{BS} \triangleq R_0^2 \frac{\hat{H}}{\hat{F}} k_{sp} \frac{Z_{eff}}{(T_e^{prof})^{\frac{3}{2}}} \left[2\mathcal{L}_{31} T_e^{prof} \frac{\partial n_e^{prof}}{\partial \hat{\rho}} + (2\mathcal{L}_{31} + \mathcal{L}_{32} + \alpha \mathcal{L}_{34}) n_e^{prof} \frac{\partial T_e^{prof}}{\partial \hat{\rho}} \right], \tag{A.19}$$

and δ_ψ is an uncertain term given by

$$\delta_\psi = \frac{\delta_\eta}{\mu_0 \rho_b^2 \hat{F}^2 \hat{\rho}} \frac{\partial}{\partial \hat{\rho}} \left(\hat{\rho} \hat{F} \hat{G} \hat{H} \frac{\partial \psi}{\partial \hat{\rho}} \right) + R_0 \hat{H} \left[\delta_{j_{ni}} \left(\frac{k_{sp} Z_{eff}}{T_e^{nom\,3/2}} + \delta_\eta \right) + \delta_\eta \left(\sum_{i=1}^{i=N_{NBI}} j_{NBI,i} + \sum_{j=1}^{j=N_{EC}} j_{EC,j} + j_{BS} \right) \right], \quad \text{(A.20)}$$

where the uncertain variables δ_η and $\delta_{j_{ni}}$ have been defined in (A.11) and (A.15), respectively. For convenience, the poloidal-flux gradient is defined as $\theta \triangleq \frac{\partial \psi}{\partial \hat{\rho}}$. Taking partial derivative with respect to $\hat{\rho}$ in (A.16) yields

$$\frac{\partial \theta}{\partial t} = \left[\left(f'_{\eta,1} f'_{\eta,2} + f_{\eta,1} f''_{\eta,2} \right) \theta + \left(f'_{\eta,1} f_{\eta,2} + 2 f_{\eta,1} f'_{\eta,2} \right) \theta' + f_{\eta,1} f_{\eta,2} \theta'' \right] u_\eta + \sum_{i=1}^{i=N_{NBI}} f'_{NBI,i} u_{NBI,i} + \sum_{j=1}^{j=N_{EC}} f'_{EC,j} u_{EC,j} + \left(\frac{f'_{BS}}{\theta} - \frac{f_{BS}}{\theta^2} \theta' \right) u_{BS} + \delta_\theta, \quad \text{(A.21)}$$

where the dependence with $\hat{\rho}$ and t has been dropped to simplify the notation, $(\cdot)' \triangleq \partial(\cdot)/\partial \hat{\rho}$, and $\delta_\theta \triangleq \delta'_\psi$. Particularizing (A.21) at $\hat{\rho} = \Delta\hat{\rho}$, for some small $\Delta\hat{\rho}$, and discretizing the spatial derivatives of θ as

$$\theta'' \approx \frac{\theta(2\Delta\hat{\rho}, t) - 2\theta(\Delta\hat{\rho}, t)}{\Delta\hat{\rho}^2}, \quad \theta' \approx \frac{\theta(2\Delta\hat{\rho}, t)}{2\Delta\hat{\rho}}, \quad \text{(A.22)}$$

where the boundary condition in (A.2) at $\hat{\rho} = 0$ (i.e. $\theta(0, t) = 0$) has been employed, provides the following equation

$$\left. \frac{\partial \theta}{\partial t} \right|_{\hat{\rho}=0} = \left\{ \alpha_0 \theta(2\Delta\hat{\rho}) + \beta_0 \left[\theta(2\Delta\hat{\rho}) - 2\theta(\Delta\hat{\rho}) \right] \right\} u_\eta + \sum_{i=1}^{i=N_{NBI}} g_{NBI,i} u_{NBI,i} + \sum_{j=1}^{j=N_{EC}} g_{EC,j} u_{EC,j} + \left(\frac{g_{BS,1}}{\theta(\Delta\hat{\rho})} - \frac{g_{BS,2}}{\theta(\Delta\hat{\rho})^2} \theta(2\Delta\hat{\rho}) \right) u_{BS} + \delta_{\theta,0}. \quad \text{(A.23)}$$

In (A.23), the time dependence within θ has been dropped to simplify the notation, $\delta_{\theta,0} \triangleq \delta_\theta(\hat{\rho} = 0, t)$, and the other variables are defined as

$$\alpha_0 \triangleq \left. \frac{f'_{\eta,1} f_{\eta,2} + 2 f_{\eta,1} f'_{\eta,2}}{2\Delta\hat{\rho}} \right|_{\hat{\rho}=0}, \quad \beta_0 \triangleq \left. \frac{f_{\eta,1} f_{\eta,2}}{\Delta\hat{\rho}^2} \right|_{\hat{\rho}=0}, \quad g_{NBI,i} \triangleq f'_{NBI,i}(\hat{\rho} = 0), \quad \text{(A.24)}$$

$$g_{EC,j} \triangleq f'_{EC,j}(\hat{\rho} = 0), \quad g_{BS,1} \triangleq f'_{BS}(\hat{\rho} = 0), \quad g_{BS,2} \triangleq \frac{f_{BS}(\hat{\rho} = 0)}{2\Delta\hat{\rho}}. \quad \text{(A.25)}$$

Using the definition of q_0 given in (2), and discretizing $\theta'(0, t) = \theta(\Delta\hat{\rho})/\Delta\hat{\rho}$, it is found that $q_0 = -\frac{B_{\phi,0} \rho_b^2 \Delta\hat{\rho}}{\theta(\Delta\hat{\rho})}$, and taking the time derivative yields

$$\frac{dq_0}{dt} = \frac{B_{\phi,0} \rho_b^2 \Delta\hat{\rho}}{\theta(\Delta\hat{\rho})^2} \frac{d\theta(\Delta\hat{\rho})}{dt} = -\frac{q_0}{\theta(\Delta\hat{\rho})} \frac{d\theta(\Delta\hat{\rho})}{dt}. \quad \text{(A.26)}$$

Using (A.23) to substitute $\frac{d\theta(\Delta\hat{\rho})}{dt}$ within (A.26), the following dynamical equation for q_0 can be written

$$\frac{dq_0}{dt} = q_0 \lambda_\eta u_\eta + q_0^2 \sum_{i=1}^{N_{NBI}} \lambda_{NBI,i} u_{NBI,i}$$

$$+q_0^2 \sum_{j=1}^{N_{EC}} \lambda_{EC,j}(\hat{\rho}_{EC,j}) u_{EC,j} + q_0^3 \lambda_{BS} u_{BS} + \delta_{q_0} \triangleq j_{q_0} + \delta_{q_0}, \tag{A.27}$$

where λ_η, $\lambda_{NBI,i}$, $\lambda_{EC,j}$, and λ_{BS} are model functions given by

$$\lambda_\eta \triangleq 2\beta_0, \quad \lambda_{NBI,i} \triangleq \frac{g_{NBI,i}}{B_{\phi,0}\rho_b^2 \Delta\hat{\rho}}, \quad \lambda_{EC,j} \triangleq \frac{g_{EC,j}}{B_{\phi,0}\rho_b^2 \Delta\hat{\rho}}, \quad \lambda_{BS} \triangleq -\frac{g_{BS,1}}{(B_{\phi,0}\rho_b^2 \Delta\hat{\rho})^2}, \tag{A.28}$$

j_{q_0} is an auxiliary variable used to denote the right-hand side of the q_0 dynamical equation without uncertainties, and δ_{q_0} is an uncertainty given by

$$\delta_{q_0} \triangleq -q_0 \frac{\theta(2\Delta\hat{\rho})}{\theta(\Delta\hat{\rho})}(\alpha_0 + \beta_0) u_\eta - q_0^3 \frac{g_{BS,2}}{(B_{\phi,0}\rho_b^2 \Delta\hat{\rho})^2} \frac{\theta(2\Delta\hat{\rho})}{\theta(\Delta\hat{\rho})} u_{BS} + \delta_{\theta,0}. \tag{A.29}$$

In addition, a dynamical model for q_e can be obtained from the boundary condition at $\hat{\rho} = 1$ in (A.2). Taking the time derivative in the definition of q_e in (2) and using (A.2), the dynamics of q_e can be described by

$$\frac{dq_e}{dt} = -B_{\phi,0}\rho_b^2 \left(\frac{1}{k_{I_p} I_p^2} \frac{dI_p}{dt} + \frac{1}{k_{I_p}^2 I_p} \frac{dk_{I_p}}{dt} \right). \tag{A.30}$$

It is considered that $k_{I_p} \triangleq \frac{\mu_0 R_0}{\hat{G}(\hat{\rho}=1)\hat{H}(\hat{\rho}=1)}$ is uncertain and can be written as $k_{I_p} = k_{I_p}^{nom} + \delta_{k_{I_p}}$, where $k_{I_p}^{nom}$ is a nominal, constant value of k_{I_p}, and $\delta_{k_{I_p}}$ is an uncertainty that characterizes modeling inaccuracies in k_{I_p}. These can arise, for example, from changes in the equilibrium factors $\hat{G}$ and $\hat{H}$ at $\hat{\rho} = 1$. Equation (A.30) can be rewritten as

$$\frac{dq_e}{dt} = -B_{\phi,0}\rho_b^2 \left(\frac{1}{k_{I_p}^{nom} I_p^2} \frac{dI_p}{dt} + \delta_{q_e} \right), \tag{A.31}$$

where δ_{q_e} is an uncertain term given by

$$\delta_{q_e} \triangleq \frac{1}{I_p^2} \frac{dI_p}{dt} \left(\frac{1}{k_{I_p}^{nom} + \delta_{k_{I_p}}} - \frac{1}{k_{I_p}^{nom}} \right) + \frac{1}{(k_{I_p}^{nom} + \delta_{k_{I_p}})^2 I_p} \frac{d\delta_{k_{I_p}}}{dt}. \tag{A.32}$$

Appendix B. Toroidal Rotation Modeling

The plasma is considered as a single particle from the point of view of classical mechanics, with mass m_p equal to the total plasma mass, which rotates at a distance R_0 in the toroidal direction with velocity $R_0\Omega_\phi$. Then, the angular momentum of the plasma is given by $L = m_p \Omega_\phi R_0^2$. Also, different contributions to the total torque T are considered, as given by

$$T = T_{NBI} + T_{int} = \sum_{i=1}^{N_{NBI}} T_{NBI,i} + T_{int}, \tag{B.1}$$

where T_{NBI} is the total NBI torque, $T_{NBI,i}$ is the contribution of the i-th NBI, which is modeled as

$$T_{NBI,i} = k_{NBI,i} P_{NBI,i}, \tag{B.2}$$

where $k_{NBI,i}$ is a parameter that models the torque deposition of the i-th NBI (e.g. $k_{NBI,i} > 0$ for co-I_p NBIs, and $k_{NBI,i} < 0$ for counter-I_p NBIs), and T_{int} is the intrinsic torque [27], which is modeled as

$$T_{int} = k_{int}\frac{W}{I_p}, \tag{B.3}$$

where k_{int} is a constant parameter. The time variation of L is given by

$$\frac{dL}{dt} = T + \delta^*_{\Omega_\phi}, \tag{B.4}$$

where $\delta^*_{\Omega_\phi}$ is an uncertain term that characterizes other unmodeled sources of torque within the plasma, and for which an upper bound can be estimated. Defining a characteristic confinement-time as $\tau_{\Omega_\phi} \triangleq \frac{m_p}{\frac{dm_p}{dt}}$, and using (B.1)-(B.3), the equation (B.4) can be rewritten as

$$\frac{d\Omega_\phi}{dt} = -\frac{\Omega_\phi}{\tau_{\Omega_\phi}} + \frac{1}{m_p R_0^2}\left(\sum_{i=1}^{N_{NBI}} k_{NBI,i}P_{NBI,i} + k_{int}\frac{W}{I_p}\right) + \delta_{\Omega_\phi}, \tag{B.5}$$

where $\delta_{\Omega_\phi} \triangleq \delta^*_{\Omega_\phi}/(m_p R_0^2)$. Finally, m_p and τ_{Ω_ϕ} are modeled as

$$m_p = m_D\frac{\bar{n}_e V}{N_{av}}, \qquad \tau_{\Omega_\phi} = k_{\Omega_\phi}\tau_E, \tag{B.6}$$

where m_D is the molar mass of the deuterium ions, N_{av} is Avogadro's number, and k_{Ω_ϕ} is a model parameter.

Appendix C. Modified Rutherford Equation

The derivation starts from the version of the modified Rutherford equation in [21],

$$\frac{\tau_R}{r}\frac{dw}{dt} = \Delta' r + a_2\frac{j_{BS}(\hat{\rho}_{NTM})}{j_\phi(\hat{\rho}_{NTM})}\frac{L_q}{w}\left(1 - \frac{w_{marg}^2}{3w^2} - \sum_{j=1}^{j=N_{EC}} K_{EC,j}\frac{j_{EC,j}^{max}}{j_{BS}(\hat{\rho}_{NTM})}\right), \tag{C.1}$$

where Δ' is the tearing stability index, $j_{EC,j}^{max}$ is the maximum of the j-th EC current deposition, $K_{EC,j}$ are parameters that model how each EC launcher affects the island growth by localized deposition, and all the other variables have been defined in Section 3.4. The factors $K_{EC,j}$ depend on the alignment of a particular EC launcher with the magnetic island O-point, so they increase when $|\hat{\rho}_{EC,j} - \hat{\rho}_{NTM}|$ becomes small enough [21]. The tearing stability index $\Delta' r$ is modeled as

$$\Delta' r = \Delta_0' r - \frac{a_2 L_q}{j_\phi(\hat{\rho}_{NTM})}\sum_j \frac{F_{EC,j}}{\delta_{EC,j}^w} j_{EC,j}^{max}, \tag{C.2}$$

where $\delta_{EC,j}^w$ is the full-width half-maximum of the j-th launcher ECCD (which characterizes the width of the EC current distribution), and $F_{EC,j}$ are functions that model how the tearing stability index changes with localized ECH&CD [21]. For convenience, $F_{EC,j}^* \triangleq \frac{F_{EC,j}}{\delta_{EC,j}^w}$ are defined.

The total EC current deposition, $j_{EC} \triangleq \sum_j j_{EC,j}$, can be expressed in terms of the contributions from active-suppression and pre-emptive-suppression launchers. It is considered that $N_{EC,pre}$ launchers are employed for pre-emptive stabilization, and that the rest of EC launchers are used for active suppression as a group. Using the model for $j_{EC,j}$ given in (A.3) with $\delta_{T_e} \equiv \delta_{n_e} \equiv 0$, j_{EC} can be rewritten as

$$j_{EC} \triangleq \sum_{j=1}^{j=N_{EC}} j_{EC,j} = \frac{T_e^{nom}}{n_e^{nom}} \left(\sum_{k=1}^{k=N_{EC,pre}} j_{pre,k}^{dep}(\hat{\rho}_{pre,k}) P_{pre,k} + j_{act}^{dep}(\hat{\rho}_{act}) P_{act} \right), \tag{C.3}$$

where $T_e^{nom} \triangleq T_e(\delta_{T_e} = 0)$, $n_e^{nom} \triangleq n_e(\delta_{n_e} = 0)$, j_{act}^{dep}, P_{act}, and $\hat{\rho}_{act}$ denote the model profile, power, and radial ECCD location, respectively, of the launchers employed for active suppression, and $j_{pre,k}^{dep}$, $P_{pre,k}$, and $\hat{\rho}_{pre,k}$ ($k = 1, ..., N_{EC,pre}$) are the model profiles, powers, and radial ECCD location, respectively, of the pre-emptive-stabilization launchers. The model parameter j_{act}^{dep} is defined from $j_{act}^{dep} P_{act} \triangleq \sum_i j_{EC,i}^{dep} P_{EC,i}$, where the summation in i is done for all the launchers that compose the active-suppression group.

Using (C.2) and (C.3), the modified Rutherford equation (C.1) can be rewritten as

$$\begin{aligned} \frac{\tau_R}{r}\frac{dw}{dt} &= \Delta_0' r + a_2 \frac{j_{BS}}{j_\phi}\frac{L_q}{w}\left(1 - \frac{w_{marg}^2}{3w^2}\right) \\ &\quad - \frac{a_2 L_q}{j_\phi}\left[\sum_k \left(F_{pre,k}^* + \frac{K_{pre,k}}{w}\right) j_{pre,k}^{max} + \left(F_{act}^* + \frac{K_{act}}{w}\right) j_{act}^{max}\right], \end{aligned} \tag{C.4}$$

where the dependence with $\hat{\rho}_{NTM}$ has been dropped to simplify the notation, and all variables associated with the active and pre-emptive launchers are denoted by the subindexes $(\cdot)_{act}$ and $(\cdot)_{pre,k}$. The model parameters F_{act}^* and K_{act}^* are defined from $F_{act}^* j_{act}^{max} \triangleq \sum_i F_{EC,i} j_{EC,i}^{max}$ and $K_{act}^* j_{act}^{max} \triangleq \sum_i K_{EC,i} j_{EC,i}^{max}$, where the summation in i is done for all the launchers that compose the active-suppression group.

Appendix D. Exponential Stability of a Second-Order Linear System

Consider the second-order linear system with initial conditions given by

$$\frac{dx}{dt} = -\frac{1}{\tau}x - K_I \int_0^t x dt, \quad x(0) = x_0, \quad \left.\frac{dx}{dt}\right|_0 = \dot{x}_0, \tag{D.1}$$

where x is the state, $\tau > 0$ is a characteristic time, $K_I > 0$ is a design constant, δ is an uncertainty, and v is an input. The solution of (D.1) depends on the value chosen for K_I. If $K_I > \frac{1}{4\tau^2}$, the solution is given by

$$x = x_0 e^{-k_1 t}\left(\cos\omega t + \frac{k_1 + \frac{\dot{x}_0}{x_0}}{\omega}\sin\omega t\right), \tag{D.2}$$

where $k_1 \triangleq \frac{1}{2\tau}$ and $\omega \triangleq \frac{1}{2}\sqrt{4K_I - \frac{1}{\tau^2}}$. On the other hand, if $K_I \leq \frac{1}{4\tau^2}$, the solution is given by

$$x = C_1 e^{-r_1 t} + C_2 e^{-r_2 t}, \tag{D.3}$$

where $r_1 \triangleq k_1 + \sqrt{\frac{1}{\tau^2} - 4K_I}$, $r_2 \triangleq k_1 - \sqrt{\frac{1}{\tau^2} - 4K_I}$, $C_1 \triangleq \frac{r_2 x_0 - \dot{x}_0}{r_1 - r_2}$ and $C_2 \triangleq \frac{r_1 x_0 + \dot{x}_0}{r_1 - r_2}$. Therefore, regardless of the value of $K_I > 0$, $x \to 0$ as $t \to \infty$, and $\|x\| \leq ke^{-bt}$, where

$k > 0$ and $b > 0$ depend on τ, K_I, x_0, and $\dot{x}_0$. The system (D.1) is exponentially stable [29] around $x = 0$, which is an equilibrium point of (D.1).

An alternative way to prove exponential stability of (D.1) is by means of Lyapunov theory. In particular, Theorem 4.10 in [29] is adapted and used here. If a function $V(x)$ (denominated Lyapunov function) can be found such that the following conditions

$$k_1\|x\|_2^a \leq V \leq k_2\|x\|_2^a, \tag{D.4}$$

$$\frac{dV}{dt} \leq -k_3\|x\|_2^a, \tag{D.5}$$

are fulfilled at all times, where $k_1 > 0$, $k_2 > 0$, $k_3 > 0$ and $a > 0$ are constants, then $x = 0$ is exponentially stable. Before starting the proof, it is convenient to define $x_1 \triangleq x$ and $x_2 \triangleq \int_0^t x dt$, and rewrite (D.1) as

$$\frac{dx_1}{dt} = -\frac{1}{\tau}x_1 - K_I x_2, \quad \frac{dx_2}{dt} = x_1, \quad x_1(0) = x_0, \quad x_2(0) = \dot{x}_0. \tag{D.6}$$

Take a Lyapunov function V_x given by the following quadratic function,

$$V_x = \frac{1}{2}x_1^2 + \frac{1}{2}\left(K_I + \frac{1}{2\tau^2}\right)x_2^2 + \frac{1}{2\tau}x_1x_2 \triangleq \frac{1}{2}[x_1x_2]Q[x_1x_2]^T, \tag{D.7}$$

where

$$Q \triangleq \begin{bmatrix} 1 & \frac{2}{\tau} \\ \frac{2}{\tau} & K_I + \frac{1}{2\tau^2} \end{bmatrix}. \tag{D.8}$$

Because $Q > 0$, its eigenvalues are also strictly positive. Therefore,

$$\lambda_1\|x\|_2^2 \leq V_x \leq \lambda_2\|x\|_2^2, \tag{D.9}$$

where $\lambda_1 > 0$ and $\lambda_2 > 0$ are the eigenvalues of Q, which is equivalent to (D.4) with $k_1 = \lambda_1$, $k_2 = \lambda_2$, and $a = 2$. To prove (D.5), take the time derivative in (D.7),

$$\frac{dV_x}{dt} = \left[\frac{\partial V}{\partial x_1}, \frac{\partial V}{\partial x_2}\right]\left[\frac{dx_1}{dt}, \frac{dx_2}{dt}\right]^T = -\frac{1}{2\tau}x_1^2 - \frac{K_I}{2\tau}x_2^2 \leq -\frac{\min(1, K_I)}{2\tau}\|x\|_2^2, \tag{D.10}$$

which is equivalent to (D.5) with $k_3 = \frac{\min(1,K_I)}{2\tau}$ and $a = 2$. Therefore, the conditions (D.4)-(D.5) are satisfied and the system is exponentially stable.

Appendix E. Boundedness of a Second-Order, Uncertain Linear System

Consider the second-order linear system with initial conditions given by

$$\frac{dx}{dt} = -\frac{1}{\tau}x - K_I\int_{t_0}^t x dt + \delta + v, \quad x(0) = x_0, \quad \left.\frac{dx}{dt}\right|_0 = \dot{x}_0, \tag{E.1}$$

where δ is an uncertainty and v is a controllable input. For simplicity, all variables are considered to be scalars, but the theorem presented here could be generalized to variables in $\mathbb{R}^n$. The main Lyapunov theorem exploited in this work for the design of robust-control laws has been adapted and particularized from Theorem 4.18 in [29]. If the Lyapunov function $V = \frac{1}{2}x^2 + \frac{1}{2}K_I\left(\int_{t_0}^t x dt\right)^2$ fulfills

$$\frac{dV}{dt} \leq -W_x(x), \quad \forall|x| \geq \mu > 0, \tag{E.2}$$

where $W_x > 0$ is continuous and $\mu < |x_0|$ is a constant, then x can be bounded as

$$|x| \leq \beta(x_0, t - t_0), \quad \forall t \in [t_0, t_0 + T], \tag{E.3}$$

$$|x| \leq \mu, \quad \forall t > t_0 + T, \tag{E.4}$$

where β is a class $\mathcal{KL}$ function (a function $f(x, y)$ is said to be a class $\mathcal{KL}$ function if: (1) it is class $\mathcal{K}$ with respect to x, (2) it is decreasing with respect to y, and (3) $\lim f(x, y)_{y\to\infty} = 0$), and $T \geq 0$ is some time that depends on x_0 and μ. Therefore, if (E.2) is fulfilled, it can be ensured that $|x|$ is transiently bounded by β and ultimately bounded by μ.

References

[1] SNIPES, J. A. et al., Nucl. Fusion **57** (2017) 125001.
[2] SNIPES, J. A. et al., Fusion Engineering and Design **89** (2014) 507.
[3] HUMPHREYS, D. et al., Phys. Plasmas **22** (2015) 021806.
[4] HULTGREN, M. et al., IFAC-PapersOnLine **50** (2017) 1997 .
[5] ZHOU, M. et al., IFAC-PapersOnLine **48** (2015) 188 .
[6] MALJAARS, E. et al., Simultaneous Control of Plasma Profiles and Neoclassical Tearing Modes with Actuator Management in Tokamaks, in *Proc. 42nd EPS Conference on Plasma Physics*, p. P1.184, 2015.
[7] RAPSON, C. J. et al., Nucl. Fusion **53** (2013) 063020.
[8] BLANKEN, T. C. et al., Nucl. Fusion **59** (2019) 026017.
[9] VU, T. et al., Fusion Engineering and Design **147** (2019) 111260.
[10] VU, T. et al., IEEE Transactions on Nuclear Science **68** (2021).
[11] KONG, M. et al., Nucl. Fusion **59** (2019) 076035.
[12] MOREAU, D. et al., Nucl. Fusion **53** (2013) 063020.
[13] BARTON, J. et al., Plasma Phys. Control. Fusion **57** (2015) 115003.
[14] RAUPP, G. et al., Fusion Engineering and Design **123** (2017) 541 .
[15] EIDIETIS, N. W. et al., Nucl. Fusion **58** (2018) 056023.
[16] MALJAARS, E. et al., Fusion Engineering and Design **122** (2017) 94 .
[17] PAJARES, A. and SCHUSTER, E., Transactions of Plasma Science **48** (2020) 1606.
[18] PAJARES, A. et al., Integrated Robust Control of Individual Scalar Variables in Tokamaks, in *Proc. 58th IEEE Conference on Decision and Control (CDC)*, pp. 3233–3238, 2019.
[19] PAJARES, A. and SCHUSTER, E., Nuclear Fusion **61** (2021) 036006.
[20] LA HAYE, R. et al., Physics of Plasmas **9** (2002) 2051.
[21] LA HAYE, R. et al., Nucl. Fusion **45** (2005) L37.
[22] PAJARES, A. et al., Actuator Management via Real-time Optimization for Integrated Control in Tokamaks, in *Proc. 46th EPS Conference on Plasma Physics*, p. P4.1096, 2019.
[23] PAJARES, A. and SCHUSTER, E., Fusion Engineering and Design **170** (2021) 112526.
[24] HINTON, F. and HAZELTINE, R., Rev. Mod. Phys. **48** (1976) 239.
[25] BUTTERY, R. J. et al., Journal of Fusion Energy **38** (2019) 72.
[26] ITER Physics Expert Group on Confinement and Transport et al., Nuclear Fusion **39** (1999).
[27] SOLOMON, W. M. et al., Phys. Plasmas **17** (2010) 056108.
[28] FERRON, J. R. et al., Nucl. Fusion **38** (1998) 1055.
[29] KHALIL, H., *Nonlinear Systems*, Prentice Hall, 3rd edition, 2001.
[30] TURCO, F. et al., Phys. Plasmas **19** (2012) 122506.
[31] BARTON, J. et al., Physics-based Control-oriented Modeling of the Safety Factor Profile Dynamics in High Performance Tokamak Plasmas, in *Proc. IEEE Conference on Decision and Control (CDC)*, pp. 4182–4187, 2013.

[32] ERBA, M. et al., Nucl. Fusion **38** (1998) 1013.
[33] TANG, W. M. et al., Nucl. Fusion **26** (1986) 1605.
[34] ONJUN, T. et al., Phys. Plasmas **9** (2002) 5018.
[35] WEHNER, W. P., Strategies for Optimal Control of the Current and Rotation Profiles in the DIII-D Tokamak, Lehigh University, 2002, (PhD Dissertation).
[36] CERFON, J. et al., Phys. Plasmas **17** (2010) 032502.
[37] SAUTER, O. et al., Physics of Plasmas **6** (1999) 2834.